

**COMPARATIVE STUDY OF ELECTRICAL PROPERTIES
OF METAL-MONOLAYER-SEMICONDUCTOR
JUNCTIONS AT MACRO AND NANO SCALES**

by

Marcus Aleksander Kuikka
B.Sc., Simon Fraser University, 2004

THESIS SUBMITTED IN PARTIAL FULFILLMENT OF
THE REQUIREMENTS FOR THE DEGREE OF

MASTER OF SCIENCE

in the
Department
of
Chemistry

© Marcus Aleksander Kuikka 2007

SIMON FRASER UNIVERSITY

Summer 2007

All rights reserved. This work may not be
reproduced in whole or in part, by photocopy
or other means, without permission of the author.

APPROVAL

Name: Marcus Aleksander Kuikka

Degree: Master of Science

Title of Thesis: Comparative Study of Electrical Properties of Metal-Monolayer-Semiconductor Junctions at Macro and Nano Scales

Examining Committee:

Dr. George R. Agnes
Chair
Professor, Department of Chemistry

Dr. Hua-Zhong(Hogan) Yu
Senior Supervisor
Associate Professor, Department of Chemistry

Dr. Vance E. Williams
Supervisor
Assistant Professor, Department of Chemistry

Dr. Karen L. Kavanagh
Supervisor
Professor, Department of Chemistry

Dr. Nancy R. Forde
Internal Examiner
Assistant Professor, Department of Chemistry

Date Approved: May 11, 2007



DECLARATION OF PARTIAL COPYRIGHT LICENCE

The author, whose copyright is declared on the title page of this work, has granted to Simon Fraser University the right to lend this thesis, project or extended essay to users of the Simon Fraser University Library, and to make partial or single copies only for such users or in response to a request from the library of any other university, or other educational institution, on its own behalf or for one of its users.

The author has further granted permission to Simon Fraser University to keep or make a digital copy for use in its circulating collection (currently available to the public at the "Institutional Repository" link of the SFU Library website <www.lib.sfu.ca> at: <<http://ir.lib.sfu.ca/handle/1892/112>>) and, without changing the content, to translate the thesis/project or extended essays, if technically possible, to any medium or format for the purpose of preservation of the digital work.

The author has further agreed that permission for multiple copying of this work for scholarly purposes may be granted by either the author or the Dean of Graduate Studies.

It is understood that copying or publication of this work for financial gain shall not be allowed without the author's written permission.

Permission for public performance, or limited permission for private scholarly use, of any multimedia materials forming part of this work, may have been granted by the author. This information may be found on the separately catalogued multimedia material and in the signed Partial Copyright Licence.

The original Partial Copyright Licence attesting to these terms, and signed by this author, may be found in the original bound copy of this work, retained in the Simon Fraser University Archive.

Simon Fraser University Library
Burnaby, BC, Canada

ABSTRACT

The electrical properties of metal-monolayer-semiconductor junctions were examined at the macroscale using mercury drop and thermally evaporated gold pad electrodes, and at the nanoscale using ballistic emission electron microscopy (BEEM) and high-resolution transmission electron microscopy (TEM). Oxide-free silicon wafers were modified with *n*-alkyl or ω -functionalized monolayers prepared via organometallic or thermal reactions. The mercury-molecule-silicon junctions displayed a clear dependence of the barrier height on both chain length and terminal functional groups of the monolayer. Measurements using thermally deposited gold contacts (i.e., gold/monolayer/silicon) yielded identical barrier heights for all monolayers, indicating that the gold atoms penetrated into the molecular layer causing a shorting of the junctions. BEEM and TEM studies showed uniform penetration of the gold atoms into the monolayer at the nanoscale. It was evident that thiol-functionalized monolayers are able to inhibit gold penetration, preserving an intact organic monolayer at the metal-semiconductor interface.

Keywords: Silicon; monolayer; interface; contact; BEEM; Hg *I-V*; Au *I-V*; molecular electronics

Subject Terms: molecular electronics; semiconductors; interfaces; metal-monolayer-semiconductor junctions

DEDICATION

To all who helped me to this beginning, and to all who saw me through until its end.

To my parents and family, my deepest gratitude. For your unyielding support, which enabled me to pursue my potential throughout my life.

To my friends both past and present, whose company has made these years worth remembering.

ACKNOWLEDGEMENTS

I would like to thank my senior supervisor Dr. Hogan Yu for giving me the opportunity to be a part of his research group. I would like to express my appreciation to the members of my Supervisory Committee, Dr. Karen Kavanagh and Dr. Vance Williams, for their helpful discussions and suggestions throughout my studies. I would further like to thank Dr. Eberhard Kielhman for proof-reading my thesis, Emelie Voisin for helping me prepare for my defence, Dr. John Bechhoefer for AFM access, and Dr. Nancy Forde for her role as internal examiner. I would like to acknowledge Wenjie Li for all BEEM and TEM imaging as well as useful discussions. My sincerest thanks go to Hidehiko Asanuma for his assistance with my experiments as well as discussions throughout the years.

Further acknowledgment must go to Craig Cooke, Richard Gafney, and Christine Wilcox (the Pomeroy lab), for their friendship and supplies, and to the past and present members of the Yu lab group for their friendship and support.

Special thanks to Bonnie Chan; amidst the toil of science, an unforeseen joy brought into my life >

TABLE OF CONTENTS

Approval	ii
Abstract.....	iii
Dedication	iv
Acknowledgements	v
Table of Contents	vi
List of Figures.....	viii
List of Tables	xi
List of Equations	xii
Glossary	xiii
Chapter 1: Introduction	1
1.1 Schottky Diodes: History and Theory	2
1.2 Organic Monolayers on Silicon.....	10
1.3 Metal-Monolayer Interactions.....	12
1.4 Objective of this thesis	17
Chapter 2: Experimental.....	19
2.1 Sample Preparation	19
2.2 Formation of Electrical Contacts.....	22
2.2.1 Formation of Mercury Drop Electrodes	22
2.2.2 Formation of Gold Electrodes via Vacuum Deposition	24
2.3 Instrumentation.....	26
2.4 Data Analysis	30
2.4.1 Macroscale $J-V$ Measurements.....	30
2.4.2 Macroscale $C-V$ Measurements	32
2.4.3 Ballistic Electron Emission Microscopy	33
Chapter 3: Structural and Spectroscopic Characterization of organic Monolayers on silicon.....	36
3.1 Atomic Force Microscopy.....	36
3.2 ATR/FT-IR.....	38
3.3 Wetting Measurements.....	43
Chapter 4: Electrical Characterization of Metal-Monolayer-Semiconductor Junctions.....	46
4.1 Electrical Characterization of Oxidized and Organically Modified Silicon Surfaces	46

4.1.1 Macroscale Electrical Characterization	47
4.1.2 Nanoscale Electrical Characterization.....	53
4.2 Electrical Properties of Metal Monolayer-Silicon Junctions: Chain Length Dependence	55
4.2.1 Macroscale Electrical Characterization	56
4.2.2 Nanoscale Electrical Characterization.....	62
4.3 Electrical Properties of Diode Junctions Constructed from Thiol- and Thioacetate-Terminated Monolayers on Silicon	64
4.3.1 Nanoscale Electrical Measurements.....	72
4.3.2 Transmission Electron Microscopy	75
Chapter 5: Concluding Remarks and Future Work	77
References:.....	80
Appendix	82

LIST OF FIGURES

<p>Figure 1-1 A metal and n-silicon in isolation (A). Movement of electrons from n-silicon to a metal upon contact resulting in depletion region devoid of mobile carriers (electrons) (B).</p> <p>Figure 1-2 Energy band diagrams for a metal and an n-type semiconductor in thermal equilibrium when (A) not in contact and (B) in contact. $E_F(M)$, E_{Vac}, $E_c(S)$, and $E_F(S)$ are the energies of the Fermi level in the metal, of the vacuum, of the conduction band of the semiconductor, and of the Fermi level in the semiconductor, respectively.....</p> <p>Figure 1-3 Charge distributions resulting from applying (A) forward bias and (B) reverse bias across a metal n-silicon junction. The positively charged ionised dopant atoms are not mobile while the negatively charged majority carriers (electrons) are able to move.</p> <p>Figure 1-4 Simplified energy band diagrams of a contact that consists of a metal and an n-type semiconductor under (A) forward and (B) reverse bias (V_F and V_R, respectively) conditions. The definitions of the remaining symbols are given in the caption of Figure 1.1. The applied bias affects the energy level E_F of the metal, and consequently the amount of band bending ($q\varphi_i$).</p> <p>Figure 1-5 Thermally initiated radical attachment of a 1-alkene to silicon.</p> <p>Figure 2-1 Schematic diagram of a mercury drop $J-V$ probe apparatus with mercury droplet contacting a silicon wafer with various surface modifying monolayers.....</p> <p>Figure 2-2 A cross-sectional optical image of a mercury droplet and it's reflection on the monolayer-modified silicon wafer. This image also shows a line separating the droplet from it's reflection, and is used to determine the mercury droplet's diameter.</p> <p>Figure 2-3 Schematic diagrams of the apparatus used to deposit gold pads onto silicon wafer.</p> <p>Figure 2-4 Schematic diagram of the gold pad $J-V$ probe apparatus. The inset shows an optical image of the probe contacting a 3-mm diameter gold pad on the surface of a C10-Si sample.....</p> <p>Figure 2-5 Schematic diagram of a ballistic electron emission microscope.....</p> <p>Figure 3-1 Contact mode AFM image of (A) SiO₂-Si and (B) C10-Si.....</p> <p>Figure 3-2 ATR-FTIR spectra of (A) C12-Si, (B) C10-Si, and (C) C8-Si samples.....</p>	<p>5</p> <p>5</p> <p>7</p> <p>7</p> <p>12</p> <p>23</p> <p>23</p> <p>24</p> <p>25</p> <p>29</p> <p>37</p> <p>40</p>
--	---

Figure 3-3	ATR-FTIR spectra for (A) C _{12T} -Si, (B) AcSC11-Si, and (C) HSC11-Si.	41
Figure 3-4	FT-IR overlay of AcSC11-Si (solid line) and HSC11-Si (dashed line) highlighting the loss of carbonyl absorption upon deprotection of AcSC11-Si.	42
Figure 3-5	Cross-sectional optical images of a typical (A) hydrophilic SiO ₂ -Si and (B) a hydrophobic C ₁₀ -Si wafer.	44
Figure 4-1	Logarithmic current density plots for H-Si, SiO ₂ -Si, and C ₁₀ -Si surfaces as measured by (A) mercury drop and (B) gold pad top electrical contacts.	47
Figure 4-2	Mott-Schottky plots depicting the behaviour of H-Si, SiO ₂ -Si and C ₁₀ -Si surfaces as measured by mercury drop (A) and gold pad (B) top electrical contacts.	51
Figure 4-3	STM topography and corresponding BEEM current images for (A) Au H-Si and (B) Au C ₁₀ -Si.	53
Figure 4-4	Static BEEM I-V curves for Au H-Si and Au C ₁₀ -Si samples demonstrating a 20% decrease in BEEM current for C ₁₀ -Si samples.	54
Figure 4-5	Log current density vs. voltage of a series of n-alkyl-modified silicon surfaces (C ₆ -Si, C ₈ -Si, C ₁₀ -Si, C ₁₂ -Si) as measured by mercury drop (A) and gold pad (B) top electrical contacts.	56
Figure 4-6	The effect of increasing chain length on the ideality factors and barrier heights of a series of n-alkyl-modified silicon surfaces (C ₆ -Si, C ₈ -Si, C ₁₀ -Si, C ₁₂ -Si) as measured by mercury drop (A and C) and gold pad (B and D) electrical contacts.	57
Figure 4-7	Diagram depicting the increasing tunnelling barrier on increasing the chain length of the monolayer in Hg C _n -Si junctions, where n is the number of CH ₂ /CH ₃ groups.	58
Figure 4-8	Mott-Schottky plots of a series of n-alkyl-modified silicon surfaces (C ₆ -Si, C ₈ -Si, C ₁₀ -Si, and C ₁₂ -Si) as measured by mercury drop (A) and gold pad (B) top electrical contacts.	60
Figure 4-9	STM topography (in nm) and corresponding BEEM current images (in pA) for a series of Au n-alkyl monolayer-silicon junctions: Au C ₆ -Si (A), Au C ₈ -Si (B), Au C ₁₀ -Si (C), and Au C ₁₂ -Si (D).	62
Figure 4-10	Static BEEM I-V curves for Au C ₆ -Si, Au C ₈ -Si, Au C ₁₀ -Si, and Au C ₁₂ -Si along with theoretical fits, (solid lines), based on Bell-Kaiser theory.	63
Figure 4-11	Log current density vs. voltage for Au C _{12T} -Si, Au AcSC11-Si, and Au HSC11-Si as measured by mercury drop (A) and gold pad (B) top electrical contacts.	66
Figure 4-12	The effect of terminal monolayer functionality on the ideality factors and barrier heights of C _{12T} -Si, AcSC11-Si, and HSC11-Si samples as measured by mercury drop (A and C) and gold pad (B and D) electrical contacts.	67

Figure 4-13 Mott-Schottky plots depicting the behaviour of n-alkyl (C_{12T} -Si), and functionalised alkyl monolayers (AcSC11-Si and HSC11-Si) as measured by mercury drop (A) and gold pad (B) top electrical contacts.....	70
Figure 4-15 STM topography and corresponding BEEM current images for (A) AcSC11-Si and (B) HSC11-Si.	72
Figure 4-16 Illustration of the behaviour of gold atoms upon thermal deposition onto (A) methyl-terminated (B) (partially) thiol-terminated monolayers on silicon. Larger green circles represent terminal thiol groups, while smaller orange circles represent gold atoms.....	73
Figure 4-17 BEEM $I-V$ overlay of Au H-Si, Au C10-Si, Au AcSC11-Si, and Au HSC11-Si showing the decreasing magnitude of BEEM current on going from un-oxidized, to n-alkyl protected, to alkyl-thioacetate protected, to alkyl-thiol protected silicon.....	74
Figure 4-18 TEM cross-sectional images of AcSC11-Si (A and B) and HSC11-Si (C and D) samples taken down the (112) and (110) dipoles respectively.....	75
Figure 5-1 AFM image and associated line profile of a HSC11-Si sample incubated with a solution of 10 nm gold particles.	79
Figure A-1 Overlay of (A) 66 $J-V$ plots for Hg C10-Si junctions and (B) 33 $J-V$ plots for Au C10-Si junctions.....	83
Figure A-2 Distributions of the ideality factors and barrier heights for extracted from current density–voltage ($J-V$) curves. Distribution of the (A) ideality factors and (B) barrier heights of 66 independent Hg C10-Si junctions from 12 C10-Si samples. Distribution of ideality factors (C) and barrier heights (D) of 33 Au C10-Si junctions from 7 C10-Si samples.....	84

LIST OF TABLES

Table 3-1	FT-IR data for Silicon modified with organic monolayers.....	40
Table 3-2	Contact angles made with 2- μ L droplets of de-ionized water on surfaces of SiO ₂ -Si, H-Si, C6-Si, C8-Si, C10-Si, C12-Si, AcSC11-Si, and HSC11-Si.	44
Table 4-1	Ideality factors (n) and barrier heights ($q\phi_{eff}$) for H-Si, C10-Si and SiO ₂ -Si as measured by mercury drop and gold pad electrical contacts.....	48
Table 4-2	The calculated dopant density (N_d), built-in potential (V_{d0}) and barrier height ($q\phi_b$) for H-Si, SiO ₂ -Si and C10-Si samples as measured by mercury drop and gold pad top electrical contacts.	51
Table 4-3	Ideality factors (n) and barrier heights ($q\phi_{eff}$) for C6-Si, C8-Si, C10-Si and C12-Si as measured by mercury drop and gold pad top electrical contacts.	57
Table 4-4	The calculated dopant density (N_d), flatband voltage (V_{d0}) and barrier height ($q\phi_b$) of a series of n-alkyl silicon surfaces (C6-Si, C8-Si, C10-Si, and C12-Si) as measured by mercury drop and gold pad electrical contacts.	60
Table 4-5	Ideality factors (n) and barrier heights ($q\phi_{eff}$) for C12 _T -Si, AcSC11-Si, and HSC11-Si samples as measured by mercury drop and gold pad top electrical contacts.	67
Table 4-6	The calculated dopant density (N_d), flatband voltage (V_{d0}), and barrier height ($q\phi_b$) of n-alkyl (C12 _T -Si), and functionalised alkyl monolayers (AcSC11-Si and HSC11-Si) as measured by mercury drop and gold pad electrical contacts.	71

LIST OF EQUATIONS

Equation 1.1	Barrier height as a function of the difference between the work function of a metal and a semiconductor's electron affinity	6
Equation 1.2	Barrier height as a function of the pinned Fermi level.....	8
Equation 2.1	Current density across a semiconductor diode junction based on thermionic emission theory.....	30
Equation 2.2	Effective barrier height due to semiconductor and a molecular tunneling barrier	31
Equation 2.3	Current density across a semiconductor diode junction based on thermionic emission theory with a molecular tunneling barrier contribution.....	31
Equation 2.4	Capacitance of a thin film insulator on a semiconductor	32
Equation 2.5	Capacitance of a thin film insulator on a semiconductor calculated using Mott-Schottky theory	32
Equation 2.6	Barrier height calculated using Mott-Schottky theory	33
Equation 2.7	Tunneling current between the STM tip and the metal contact in a ballistic electron emission microscope	34
Equation 2.8	Collector current for a ballistic electron emission microscope	34
Equation 2.9	Collector current in a ballistic electron emission microscope in terms of the tunneling current.	35
Equation 3.1	The intensity of an evanescent wave as a function of the distance from the surface of an ATR crystal	39
Equation 4.1	Barrier height with added contribution of molecular dipole moment	69
Equation 4.2	Molecular dipole as a function of the molecules dipole moment and orientation on the surface.....	69

GLOSSARY

AFM	atomic force microscopy
FT-IR	Fourier transform infrared spectroscopy
BEEM	ballistic electron emission microscopy
NTP	nano-transfer printing
TEM	transmission electron microscopy
<i>J-V</i>	current density-voltage measurement
<i>C-V</i>	capacitance-voltage measurement
<i>M-S</i>	Mott-Schottky measurement
ATR	attenuated total reflectance
STM	scanning tunnelling microscopy
<i>n</i>	ideality factor
$q\phi_{eff}$	effective barrier height
E_F	Fermi energy level
$E_F(M)$	Fermi energy level of metal
E_{Vac}	energy of vacuum
$E_c(S)$	energy of conduction band of semiconductor
$E_F(S)$	Fermi energy level of semiconductor
MCT detector	mercury-cadmium-telluride detector

CHAPTER 1: INTRODUCTION

Few industries have altered the fundamental aspects of how people operate in the world as much as the semiconductor industry: from the development of computers capable of rapid and large calculations, to advances in communications and even to the exploitation of new energy sources. With the performance of many materials in semiconductor devices approaching their theoretical limits, researchers are turning towards the emerging field of molecular electronics for solutions. By combining the properties of vast libraries of organic molecules with the materials widely used in the semiconductor industry, it is becoming possible to create devices such as transistors^{1, 2}, optically-active switches³, and diodes⁴ which surpass the limits of conventional materials and even to develop novel applications^{5, 6}.

The development of practical molecular electronic devices such as diodes and transistors for the market is however still in its infancy, with many fundamental questions remaining. Of particular interest is the electrical behaviour at the interface between modifying organic molecules and semiconductor substrates and whether conventional fabrication techniques, such as vapour deposition of metal contacts, can be applied to molecular electronics. The aim of this thesis project was to investigate the effect of different types of metal contacts in metal-monolayer-semiconductor Schottky diodes. Chapter 1 introduces Schottky diodes and semiconductor theory, the use of monolayers on semiconductor materials, and the interaction of metals with monolayers. Chapter 2 describes the experimental methods. Chapter 3 presents experimental data showing the

structural and spectroscopic characterization of the organic monolayers on silicon. Chapter 4 presents experimental data for the electrical characterization of modified silicon junctions. Chapter 5 provides concluding remarks and suggests future work.

1.1 Schottky Diodes: History and Theory

Semiconductors are made of elements (such as silicon) and compounds (such as lead sulfide, PbS, or gallium arsenide, GaAs), whose conductivity is intermediate to that of metals and insulators. This property is a result of the band structure of the semiconductors, the allowed energy levels that electrons may occupy, determined by the overlap of the atomic orbitals of the individual atoms in the bulk material. For semiconductor materials, electrons are confined to two bands of energy, the conduction band and the valence band, with the two bands being separated by a region of forbidden electron energies called the band gap. Electrons in the valence band are fixed while those in the conducting band are mobile. The ability of electrons to get into the conduction band, and hence become conductive, depends on their ability to cross the band gap. The usefulness of semiconductors arises from the ability to control their conductivity, effectively the number of electrons in the conduction band, by exposure of the semiconductor to different temperatures, electric currents, electromagnetic fields, and even light.

One of the key devices of the semiconductor industry that exploits the electronic properties of semiconductors is the rectifier, or diode. Developed from research on the electrical flow between metal contacts and various oxides and sulphides, the first diode was described in 1874 by Carl Ferdinand Braun⁷. While studying the electrical behaviour between lead sulphide and flattened silver wires, Braun discovered that the resistance of

the device varied with the direction, intensity and duration of the current. Braun soon discovered that the rectifying phenomenon could be enhanced if sharpened tips of metal were used in place of the flattened wires, leading to the development of the point-contact diode.

The first applications for diodes came about after the detection of radio waves by Hertz in 1887. The first diode radio detector consisted of a springy phosphor bronze wire in a holder, which an operator could place in contact with an oxide or sulphide crystal (such as galena, PbS). The diode would receive an AM radio signal and rectify it, producing an averaged voltage, which would then be amplified and sent to a transducer; the latter would then produce a sound signal. This was also the point at which silicon electronic devices made a brief entry into the commercial market with the introduction of a radio wave detector by Pickard in 1907. Despite these initial advances, research on semiconductor technology waned rapidly with the development of the more reliable vacuum electron tubes. As a result, the modern era did not really begin until 1939 when Russel Ohl began purifying silicon in an attempt to produce more reliable point contact diodes. In this process, impurities within the silicon separated and distributed themselves in such a way that some areas of the silicon now had an excess of electron donating atoms (n-type) and others a deficit (p-type). Electrons from the n-type side would then flow into the acceptor-rich p-type side and the two would cancel each other out. This leaves a region devoid of any moving charges, a depletion zone. Any electrons that try and cross this depletion zone would see a region of positive charge on the n-type side, and a region of negative charge on the p-type side and as result, a barrier to $n \rightarrow p$ electron movement, a rectifying barrier, was created.

While the development of diodes was begun in the early 1870's, theories explaining the rectifying behaviour of semiconductor materials did not appear until 1931 when Schottky, Stormer, and Waibel postulated a potential barrier at the metal/semiconductor interface after observing that the potential drop occurred almost entirely at the contact⁸. In 1938, Schottky^{9, 10} and Mott^{11, 12} independently showed that the rectifying behaviour of diodes was due to a potential barrier for electrons travelling from the semiconductor into the metal, formed as a result of differences in the work functions of the metal and the semiconductor. The work function is defined as the energy required to remove an electron from the Fermi level to vacuum, where the Fermi energy level at 0 K is defined as the energy at which available electron states are occupied and at higher temperatures, it is the energy at which the probability of a state being occupied is 0.5. In a metal, the highest occupied electron band is half-filled so that the Fermi level is within an allowed band, and the electron density is very high, allowing for a high conductivity. In a semiconductor, the Fermi level is located within the band gap of the semiconductor, and the energy required to remove an electron is a function of the material's electron affinity. When the metal and the semiconductor are brought into contact with each other, their Fermi levels necessarily need to align themselves. When the two materials are brought into contact with each other, electrons will flow from the conduction band of the semiconductor into the metal forming a depletion region in the semiconductor where majority carriers have been depleted (Figure 1-1). This results in the bending of the semiconductor bands and a barrier to electron transport across the interface (Figure 1-2).

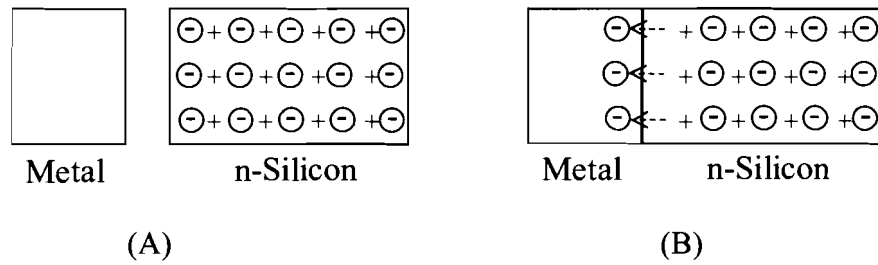


Figure 1-1 A metal and n-silicon in isolation (A). Movement of electrons from n-silicon to a metal upon contact resulting in depletion region devoid of mobile carriers (electrons) (B).

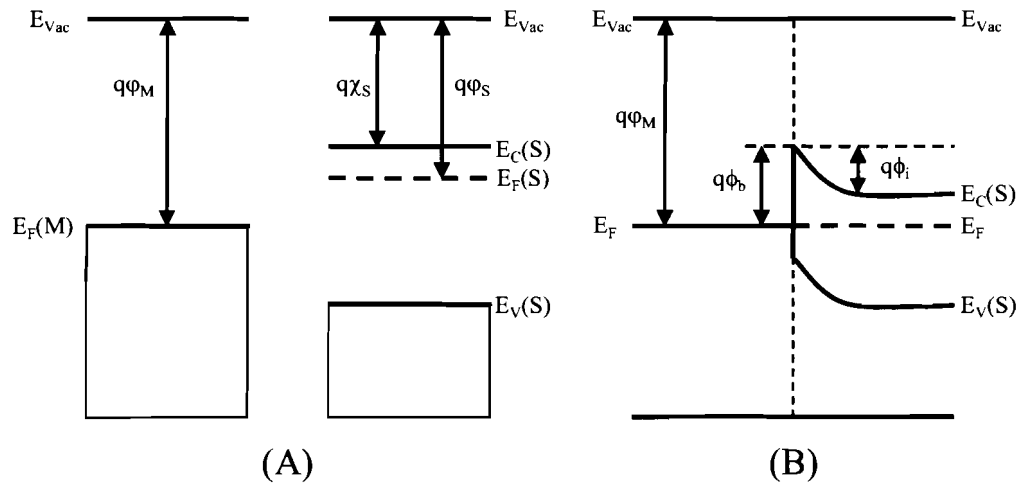


Figure 1-2 Energy band diagrams for a metal and an n-type semiconductor in thermal equilibrium when (A) not in contact and (B) in contact. $E_F(M)$, E_{Vac} , $E_c(S)$, and $E_F(S)$ are the energies of the Fermi level in the metal, of the vacuum, of the conduction band of the semiconductor, and of the Fermi level in the semiconductor, respectively¹³.

The barrier height can then be calculated from the difference between the work function of the metal and the semiconductor's electron affinity¹³:

$$q\phi_b = q(\varphi_m - \chi_s) \quad \text{Equation 1.1}$$

where q is the elementary charge, ϕ_b is the Schottky barrier height, φ_m is the metal work function, and χ_s is the electron affinity of the semiconductor.

Figures 1-3 and 1-4 show the effect of applying a potential bias across a metal|n-silicon junction. When a forward bias is applied (semiconductor is negative with respect to the metal), electrons will accumulate in the space charge region, resulting in a lower barrier height. When a reverse bias is applied across the junction (semiconductor is positive with respect to the metal), electrons will move away from the space charge region, resulting in a larger barrier height.

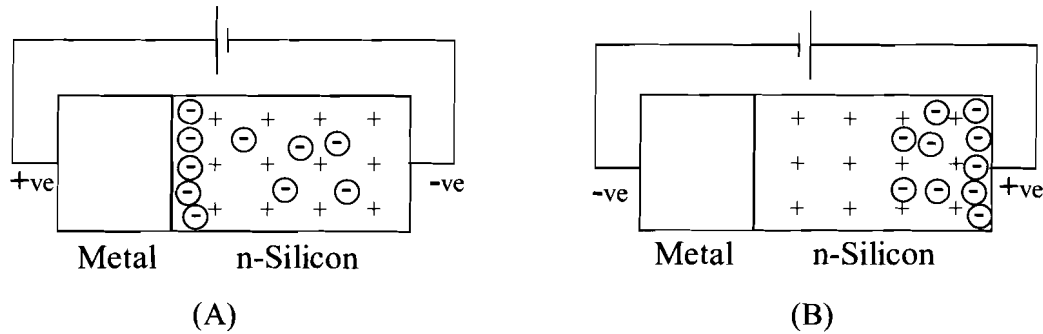


Figure 1-3 Charge distributions resulting from applying (A) forward bias and (B) reverse bias across a metal | n-silicon junction. The positively charged ionised dopant atoms are not mobile while the negatively charged majority carriers (electrons) are able to move.

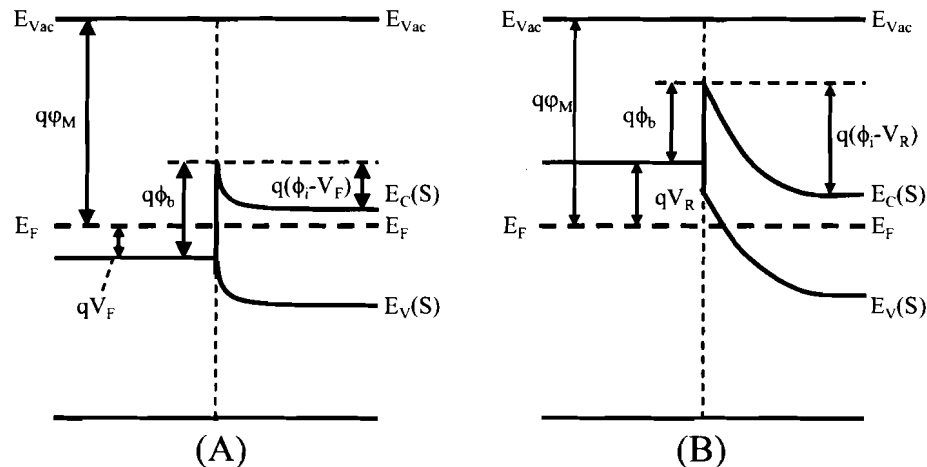


Figure 1-4 Simplified energy band diagrams of a contact that consists of a metal and an n-type semiconductor under (A) forward and (B) reverse bias (V_F and V_R , respectively) conditions. The definitions of the remaining symbols are given in the caption of Figure 1.1. The applied bias affects the energy level E_F of the metal, and consequently the amount of band bending ($q\phi_i$)¹³.

According to equation 1.1, the barrier height should vary linearly with the metal work function, and it should be possible to tune the barrier height of a diode by substituting the metal contact with another of a different work function. Experimentally, however, it is found that control over the barrier height in this fashion is limited to ionic

semiconductors, with relations between $q\phi_b$ and $q\varphi_M$ in covalent semiconductors being weak to nonexistent¹⁴⁻¹⁶. Bardeen proposed an explanation of this observation by postulating that localized surface states of the semiconductor determine the barrier height¹⁷. In a bulk semiconductor, the distribution of electronic states of the valence electrons is determined by the periodic arrangement of the atoms in the crystal. In effect, the electrons are localized in the spaces between neighbouring atoms. This localization of electrons leads to band gaps. On reaching the surface of the semiconductor, there are no longer any atoms with which to form covalent bonds leaving “dangling bonds” of unpaired electrons. These dangling bonds give rise to energy states, called surface states that may exist within the band gap. Because of the existence of these energy states within the gap, the Fermi level is pinned. Now when the metal and semiconductor are brought into contact, the exchange of charge occurs between the metal and the surface states, and the barrier height can be determined by the position of the now pinned Fermi level¹³:

$$q\phi_b = q(E_c - E_F)$$

Equation 1.2

where q is the elementary charge, E_c is the conduction band edge position and E_F is the pinned Fermi level.

Other considerations when examining the nature of the energy states at the interface arise from making the actual metal contact with the semiconductor surface. Heine pointed out that it is possible for the wave functions of metal electrons to enter the region of the semiconductor band gap¹⁸. If this were to occur, these metal-induced gap

states (MIGS) would overshadow the intrinsic electronic states of the semiconductor and determine the barrier height.

It is also possible for interfacial reactions to occur between the deposited metal and the semiconductor surface resulting in the formation of metal silicides, a compounds containing silicon and a more electropositive metal atoms (i.e., PtSi). The result of such reactions, which come about by the interdiffusion of the metal and the semiconductor, is the disruption of the clean metal-semiconductor interface to an extent where the barrier height is no longer determined by the work function of the metal and the semiconductor surface properties. While the diodes still show near ideal behaviour (ideality factors ~ 1.1), the determining factor for the barrier height is now the heat of formation of the silicides.

One solution that has permitted a great degree of control over barrier height through choice of metal is the formation of a passivation layer between the metal and the semiconductor. The passivation layer of choice in the case of silicon consists of thermally grown oxides. Oxides will spontaneously form on the surface of silicon upon exposure to air. In fact, in order to prevent oxide formation, the silicon wafer would have to be cleaved, and the metal deposited under ultra high vacuum conditions. The formation of the oxide on the silicon surface satisfies all of the requirements of a passivation layer:

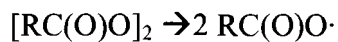
- 1) Dangling bonds are eliminated by the formation of covalent linkages between silicon and oxygen, hence reducing the number of surface states.
- 2) The probability of MIGS formation is reduced because the metal is no longer in contact with the semiconductor.

3) The separation of the metal and semiconductor results in the metal no longer being free to diffuse into the bulk semiconductor to form silicides.

1.2 Organic Monolayers on Silicon

While the thermal growth of oxide layers has been and continues to be the primary method of passivation for silicon semiconductor devices, there are several problems with its use. First, while the thickness of the oxide can be controlled down to a level of several angstroms, the oxide layer will tend to grow thicker over time. A thicker layer would result in a decrease in electron tunnelling probability and hence a decreasing current that crosses the interface as the device ages. Secondly, several metals are capable of diffusing across the oxide layer to interact with the semiconductor forming silicides and possibly MIGS. In addition, the presence of oxygen at the interface can trap charges on the surface.

An alternative to oxides in the passivation of silicon devices is the formation of covalently linked organic monolayers on the semiconductor surface. These monolayers on silicon, first prepared by Linford et al¹⁹ in 1993 with the covalent attachment of an n-alkyl monolayer to a H-Si surface with diacyl peroxides through Si-C bonds, were found to be thermally and chemically stable under a large variety of conditions^{20, 21}. The proposed reaction mechanism¹⁹ involves the diacyl peroxides ($[CH_3(CH_2)_nC(O)O]_2$, n = 16 or 10) undergoing homolytic cleavage to form two alkoxy radicals:



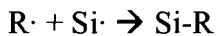
This is followed by decarboxylation forming alkyl radicals



The alkyl radical can then abstract a hydrogen atom from the surface forming a silicon radical:



which could then react with a second alkyl radical to form the monolayer



Additional reaction protocols for the preparation of organic monolayers on silicon have been developed in the past decade. Among them are photochemical^{22, 23}, metal complex-catalysed (including Grignard reactions)^{24, 25}, thermal²⁶, and electrochemical²⁷ routes.

Similar to the diacyl peroxide-promoted reaction, the first step in a thermally initiated radical reaction mechanism is hydrogen abstraction from the silicon surface, accomplished by heating the silicon substrate to a temperature greater than 150 °C, which cleaves the H-Si bond, and resulting in a silicon-dangling bond. Following activation of the surface, an alkene reacts with the silicon-dangling bond to form a surface-bound secondary carbon radical. This radical can then go on to either abstract hydrogen from another alkene molecule or from a neighbouring H-Si group, the end result being a covalently bound monolayer formed by a self-propagated chain reaction¹⁹.

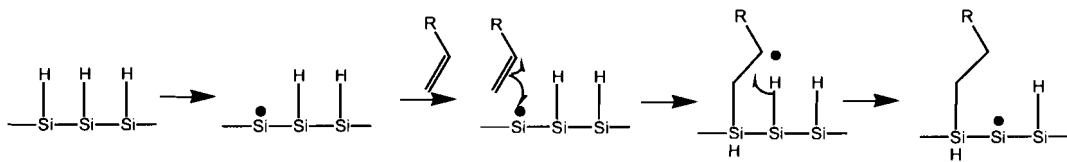


Figure 1-5 Thermally initiated radical attachment of a 1-alkene to silicon.

1.3 Metal-Monolayer Interactions

The successful development of molecular electronic devices with deposited metal contacts requires an understanding of the nature of interaction between the metal and the monolayer. In particular, how does the deposition of a metal onto a monolayer-substrate construct affect the electrical performance and the physical structure of the device, particularly at the interface between metal-monolayer and monolayer-substrate? Some possibly detrimental situations that must be addressed include: penetration of the monolayer by the deposited metal that results in shorting of the device, displacement of the monolayer from the substrate by the metal, and physical destruction of the monolayer either at the interface with the substrate or along the chain of the molecule.

Self-assembled, alkanethiolate monolayers on gold have been the focus of numerous studies examining the effect of metal deposition. Their usefulness arises from the versatility displayed by the system due to its self-assembled nature and the simplicity of forming densely packed monolayers with a variety of terminal functional groups. The connection between the monolayer and the gold substrate consists of the sulfur atom of the terminal thiol group bonding to three gold atoms on the substrate. This bond is weak enough to allow the molecules mobility on the surface as well as allow other thiolated molecules with various functional groups to be inserted into the initial monolayer. These functionalised surfaces can be used to design sensors with electrical, electrochemical, or

optical detection methods. Despite the ease of fabrication and modification of Au|SAM systems, when making top metal contacts (e.g., by thermal deposition of a metal) the mobility of the molecules on the gold substrate results in the metal penetrating into the monolayer and displacing it.

One of the primary interests in studying the properties of metal-monolayer-semiconductor junctions is to develop devices that combine easily tuneable properties of organic molecules with the readily available semiconductor processing techniques. While the most common material in use today is silicon, other semiconducting materials with established infrastructure exist such as GaAs, on which thiolated molecules self-assemble forming monolayers, similar to Au|SAM systems. This allows the characterization and an understanding of metal-monolayer-semiconductor devices using well-developed metal-insulator-semiconductor theories.

Li et al. studied the effect of introducing an alkanedithiolate molecular layer onto the surface of GaAs²⁸. The top contacts were made by using both e-beam evaporation as well as nano-transfer printing (nTP) of gold. The authors studied their systems with a ballistic electron emission microscope (BEEM), an instrument that is capable of electrical measurements down to a resolution of 1 nm. They concluded that the measured barrier height, for both the evaporated and nTP devices, clearly increased on addition of the dithiolate molecular layer. The implication of this study is that in contrast to dithiol systems on gold, where the molecules are highly mobile on the surface, dithiol layers on GaAs inhibit the penetration of the metal, resulting in a “clean” metal-insulator-semiconductor device.

Several important observations can be extracted from studies of systems where the monolayers are not strongly bound to the substrate such as thiolate SAMs on metals such as gold and on semiconductors such as gallium arsenide. Firstly, the metals are capable of penetrating into monolayers. The degree of penetration into a monolayer depends on the metal being deposited, the bonding to the substrate, as well as the terminal group of the monolayer. Secondly, because the monolayers are not strongly interacting with the substrate and therefore mobile, metals that penetrate to the monolayer/substrate interface can displace the molecules on the surface resulting in a new system of metal-monolayer-metal-substrate.

Clearly interaction between the monolayer and the substrate is of key importance, and an apparent solution would be the use of monolayers that are more strongly bound to the surface, e.g., with covalent bonds. One such system that has been studied for its potential use in molecular electronics devices uses silicon as substrate and involves monolayers covalently linked to thermally grown oxide on silicon and monolayers covalently linked to silicon via Si-O-C linkages.

Jun et al.³ studied such systems by attenuated total reflection (ATR) FT-IR spectroscopy. They immersed a silicon ATR (50×10×1 mm) crystal with native oxide into a solution of octadecyltrichlorosilane to form a monolayer linked to the silicon via a C-O-Si(Si₃) linkage. They then deposited a gold layer of 80 nm thickness at a rate of 0.1 nm/s onto either the bare monolayer or on top of a deposited adhesion layer of Cr or Ti. They were then able to pass an IR beam through the crystal, collecting absorbance information on the symmetric and asymmetric CH₂ stretches as well as the asymmetric CH₃ stretch. They observed that on deposition of the metal, upward shifts of 2-3 cm⁻¹

occurred in the ν_s and ν_a stretching frequencies of CH_2 , indicative of increasing disorder of the alkyl chains. There was also a significant broadening of the peaks, which is attributed to both increasing disorder of the monolayer (upward shift) and to interaction of the CH_2 groups with the metal (downward shift). When a layer of Ti or chromium was deposited prior to the gold layer, there was less broadening of the peaks, which the authors attributed to the Ti and Cr forming carbides reducing the ability of the deposited gold to interact with remaining alkyl chains.

Richter et al.^{29, 30} utilized a different spectroscopic technique to investigate the effect of metal deposition on the same system, namely p-polarized backside reflection absorption infrared spectroscopy (pb-RAIRS). While this system is not as sensitive to the monolayers on the surface as ATR FT-IR is, due to the single-reflection of the IR beam, special substrate shapes such as an ATR crystal are not required and the frequency range of detection is not restricted by multiphonon absorption (a quantized mode of vibration occurring in a rigid crystal lattice which may be IR active). Their studies involved cleaning double-side polished p-doped Si wafers ($8\text{-}12 \Omega\cdot\text{cm}$), removal of the native oxide via a buffered oxide etch, and then thermal oxidation of the surface. To form the monolayer, the oxidized Si wafers were immersed in 2 mM solutions of octadecyltrichlorosilane (OTS) in hexadecane for 18 hours before cleaning. For monolayers directly linked to the Si surface, the oxide was etched from the surface of the Si, followed by UV-initiated radical attachment of octadecyl alcohol in CH_2Cl_2 . The actual collection of IR data involves directing an IR beam through a $\text{SiO}_2\text{-Si-SiO}_2$ -monolayer-metal sample. Since silicon is transparent to IR and the metal reflects the IR signal, the absorption due to the monolayer can be measured. By monitoring the

stretching frequencies of the alkyl chains, a shift in the asymmetric CH₂ stretch to higher wavelengths was observed on deposition of gold or aluminum, while the intensities remained constant, which indicated a disordering of the monolayers. They also observed a weak stretch at 2825 cm⁻¹, which they attributed to an interaction of the methylene groups with the deposited metal, meaning that the deposited metals penetrated into the monolayer film but did not destroy it. It was also found that if Ti was deposited onto the monolayer surface, there was a significant decrease in the intensities of the CH₂ stretching frequencies, consistent with previous studies that suggest the highly reactive Ti reacts and partially consumes the monolayer. These results contrast directly with the studies of monolayers directly attached to bare silicon via ether linkages. No matter which metal was deposited, the resulting spectra showed no absorption due to the monolayer whatsoever. Qualitative electrical characterization also indicated that there was a direct linkage between the silicon and the deposited metal. Since the monolayer structures were identical in both cases, it became clear that the resulting differences in metal interaction were due to structural changes at the interface between the monolayer and the substrate. In the case of the OTS monolayer on thermally grown oxide, the linkage between monolayer and silicon is C-Si(OSi₃) while the octadecyl alcohol is linked via C-O-Si(Si₃) bonds. The authors proposed that Si-Si bonds were cleaved upon metal deposition due to the polarity of the Si-O bonds, which have been shown to activate adjacent molecules.

Liu and Yu carried out comprehensive studies on the electrical performance of alkyl monolayers covalently attached to silicon using a “soft” mercury metal contact. They characterized a series of n-Si-C_nH_{2n+1}-Hg MIS devices (where n=6,8,10,12)³¹ and

compared n-Si-C₁₀H₂₁|Hg with n-Si-SiO₂|Hg³², p-SiC₁₂H₂₅|Hg devices with p-Si-SiO₂|Hg, and p-Si-SiO₂-SiO₃C₁₂H₂₅|Hg with p-H-Si|Hg³³. These studies demonstrated the tuneability of the electrical behaviour of molecularly modified semiconductor junctions when a “soft” mercury drop contact is used.

1.4 Objective of this thesis

Previous studies have shown that for monolayers covalently bonded either to an oxide on silicon or directly to silicon via a Si-O bond, direct thermal metal deposition does cause at the very least a disruption in the ordering of the monolayer. Also highlighted was the importance of the interfacial chemistry between the monolayer and the substrate: the type of monolayer binding, even when strong enough to immobilize the monolayer (as opposed to “mobile” Au-S bonding), determines whether the metal will displace the monolayer. Equally important is the chemical interaction of the terminal groups of the monolayer with the incoming metal, with C=O bonds appearing to directly interact with thermally deposited gold.

While studies of thermally deposited metals on monolayers linked to silicon via Si-O bonds and of soft mercury drop contacts on monolayers linked to silicon via Si-C bonds have been carried out, no comprehensive examination of the electrical behaviour of thermally deposited metals on monolayers covalently linked to silicon via Si-C bonds have been carried out. Since the proposed mechanism for monolayer destruction on covalently linked monolayers involves the polar Si-O bond, changing the nature of this bonding may be key to creating molecular electronic devices using thermally deposited metals. In addition, the effect of monolayers covalently linked via Si-C bonds and

containing terminal functional groups that are strongly interacting with metal contacts has not been examined.

We chose to study a system of organic monolayers consisting of various chain-length alkyl groups that were covalently linked to silicon by Si-C bonds (via Grignard or thermally initiated radical reactions). Not only does this satisfy the requirement that the bonds must be strong enough to make the monolayers immobile (Si-C bond energy of 369 kJ/mol), but the polarity of the bonds is less than that of the Si-O bond, which was theorized to be the cause of monolayer destruction when metals were deposited in the covalently linked octadecyl alcohol-Si system. The effect of strongly interacting terminal functional groups on the monolayer properties was examined by introducing thioacetate and thiol groups. Electrical characterization was the key analytical technique used to probe the metal-monolayer-semiconductor structures created. Using both soft non-penetrating contacts (mercury drop) and thermally deposited gold pads, the electrical characteristics were examined at the macroscale (mercury drop J - V probe and gold pad J - V probe) and on the nanoscale (ballistic emission electron microscopy and transmission electron microscopy).

CHAPTER 2: EXPERIMENTAL

2.1 Sample Preparation

Silicon <111> wafers (0.5-5.0 Ω·cm, n-type, Virginia Semiconductor Inc.) were cleaned and modified with the following procedures. The silicon wafers were cut into 1 × 2 cm² pieces and sonicated, polished side down, with 95% ethanol for 2 minutes followed by sonication with de-ionized (DI) water (> 18.3 Ω·cm, Barnstead EasyPure UV/UF compact water system, Dubuque, IA) for a further 2 minutes. After drying in a stream of N₂ gas, the wafers were immersed, face down, in a “piranha” solution (a 3:1 mixture of concentrated H₂SO₄ and 30% H₂O₂; GEM Microelectronic Materials, Inc., Chandler, AZ) and heated to 90 °C for 30 minutes. The samples were then removed from the piranha solution and rinsed with copious amounts of DI water. Following cleaning, the native oxide was then removed by immersion, polished surface down, into ppb-grade NH₄F (40% aqueous solution degassed by bubbling Ar for at least 20 minutes, GEM Microelectronic Materials, Inc., Chandler, AZ) for 8 minutes, resulting in a hydrogen-terminated silicon surface (H-Si). Typically, H-Si surfaces were characterized immediately upon removal from the etching solution.

Oxidized silicon samples were prepared by treating the H-Si wafer in piranha solution for 30 minutes, followed by copious rinsing with DI water, and drying under a stream of N₂.

Organic modification of the silicon surfaces was accomplished by either thermal reactions with Grignard reagents³⁴, or thermally initiated radical reactions with 1-alkenes³⁵.

- 1) For the series of n-alkyl monolayers ($\text{Si-C}_n\text{H}_{2n+1}$, n = 6, 8, 10 and 12) the freshly prepared H-Si wafer was placed into a Schlenk tube containing n-alkylmagnesium bromide (5 mL, 0.5-2.0 M solution in diethyl ether; degassed by bubbling Ar for at least 20 minutes, Aldrich, Milwaukee, WI) and heated in a sand bath at 90 °C for 12 hours. The monolayer-modified wafer was cleaned by rinsing at room temperature with a 1% CF_3COOH in tetrahydrofuran (THF) (Caledon Laboratories, Ltd. Georgetown, ON), sonicating with water, sonicating in 1,1,1-trichloroethane dried by a stream of N_2 , and placed briefly in an oven at 90° C before further characterization.
- 2) Preparation of $\text{H}_3\text{COCS}(\text{CH}_2)_{11}\text{-Si}$ (AcSC11-Si) samples was accomplished using a thermally initiated radical reaction of a H-Si wafer with ω -undecenyl thioacetate. The synthesis of the precursor was based on a reported procedure³⁶. Briefly, 25 mL of ethanol and 1.7 g potassium thioacetate (Aldrich, Milwaukee, WI) were placed into a flame-dried 50-mL dual-neck round-bottom flask equipped with a condenser. ω -Undecenyl bromide (3 g, Aldrich, Milwaukee, WI) was then added, the system was flushed with Ar, then sealed. The mixture was heated to reflux and reaction progress was monitored using thin-layer chromatography (TLC). When reaction was complete, 100 mL of de-ionized water was added and the product was extracted with 3 × 50 mL portions of ether (Aldrich, Milwaukee, WI). The extracts were dried over MgSO_4 (Aldrich, Milwaukee, WI), and then passed through a filter before removing the solvent on a rotovap. The product was

further purified using flash chromatography (35:1 hexanes to ethyl acetate, (Aldrich, Milwaukee, WI).

After removing the silicon wafer from the etching solution (NH_4F), it was immediately placed into a Schlenk tube containing 5 mL of ω -undecenyl thioacetate (degassed by bubbling Ar for at least 20 minutes). The system was flushed with Ar for a further 15 minutes before being placed into a sand bath set at 200 °C for 4 hours. The wafer was then removed and cleaned by sonicating in CH_2Cl_2 (Aldrich, Milwaukee, WI), water, and again in CH_2Cl_2 before drying in a stream of N_2 .

3) $\text{HS}(\text{CH}_2)_{11}\text{-Si}$ (HSC11-Si) samples were made by in-situ reduction of the terminal - SCOCH_3 group of a AcSC11-Si sample. The AcSC11-Si sample prepared as described above was placed, polished side down, into a 10% solution of NH_4OH (degassed by bubbling Ar for at least 20 minutes, ULSI grade, GEM Microelectronic Materials, Inc. Chandler, AZ) for 20 minutes. The sample was then removed, rinsed with water, sonicated with CH_2Cl_2 and water, then rinsed with CH_2Cl_2 again before drying in a stream of N_2 , and placed briefly in an oven at 90° C to dry.

4) For comparison, silicon modified with dodecyl monolayers was also prepared via thermal routes. After removing the native oxide from a cleaned silicon wafer, the H-Si wafer was immediately placed into a Schlenk tube containing 5 mL of 11-undecene (degassed by bubbling Ar for at least 20 minutes, Aldrich, Milwaukee, WI). The system was flushed with Ar for a further 10 minutes before being placed into a sand bath set at 200 °C for 4 hours. The wafer was then removed and cleaned by sonicating in CH_2Cl_2 , water, and again with CH_2Cl_2 before drying in a stream of N_2 .

2.2 Formation of Electrical Contacts

In order to carry out electrical measurements on the modified silicon wafers, it was necessary to provide two electrical contacts, one on the backside of the silicon wafer, and the other on the surface of the monolayer. Back contacts were made by scoring the unpolished backside of the wafer with a diamond-coated pen, then using a cotton swab to coat the exposed silicon surface with an InGa eutectic (99.99 %, Aldrich). The wafer was then placed onto a copper plate that connected to a computer-controlled potentiostat. Two types of top electrical contacts were used:

- 1) Platinum wire that was immersed in a mercury-filled syringe from which a mercury droplet was extruded onto the surface of the silicon wafer.
- 2) A metal probe placed on a micro-positioning system that was lowered into contact on a thermally evaporated gold pad on the surface of the silicon wafer.

2.2.1 Formation of Mercury Drop Electrodes

A drop of mercury was extruded from a gas-tight syringe and then slowly lowered onto the surface of the silicon wafer (Figure 2.1). The approach of the mercury drop to the substrate was monitored via a digital video microscope with a 40 \times objective (Model: DM143, Micro-Optic Industrial Group Co., Hong Kong); once contact was established, an image of the droplet was taken. Using the Motic Images 2000 software provided by the manufacturer, this image was then used to measure the diameter of the droplet and calculate the area of contact. Typical diameters were between 500 and 800 μm with a 20- μm uncertainty for a 600- μm diameter droplet. After a measurement was taken, the

mercury drop was withdrawn from the surface and ejected into a waste container. Scans were repeated 6-10 times on each sample, using a fresh mercury drop each time at a different location on the sample.

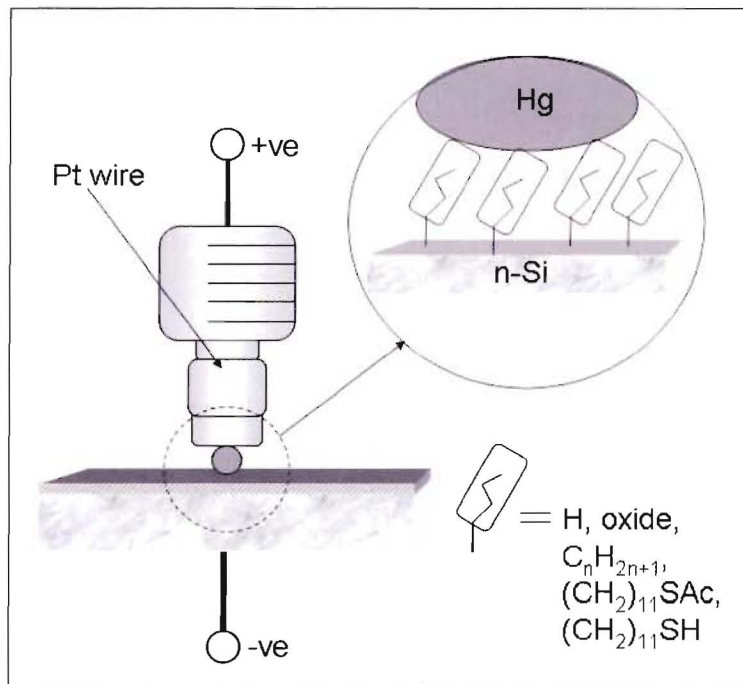


Figure 2-1 Schematic diagram of a mercury drop *J-V* probe apparatus with mercury droplet contacting a silicon wafer with various surface modifying monolayers.

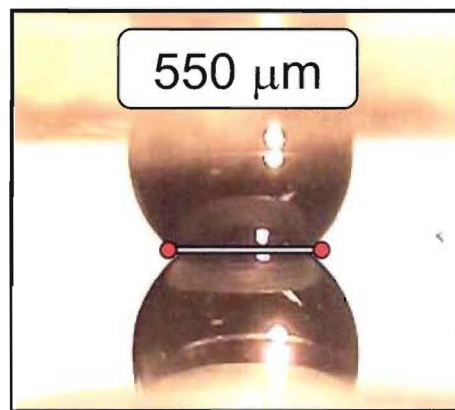


Figure 2-2 A cross-sectional optical image of a mercury droplet and it's reflection on the monolayer-modified silicon wafer. This image also shows a line separating the droplet from it's reflection, and is used to determine the mercury droplet's diameter.

2.2.2 Formation of Gold Electrodes via Vacuum Deposition

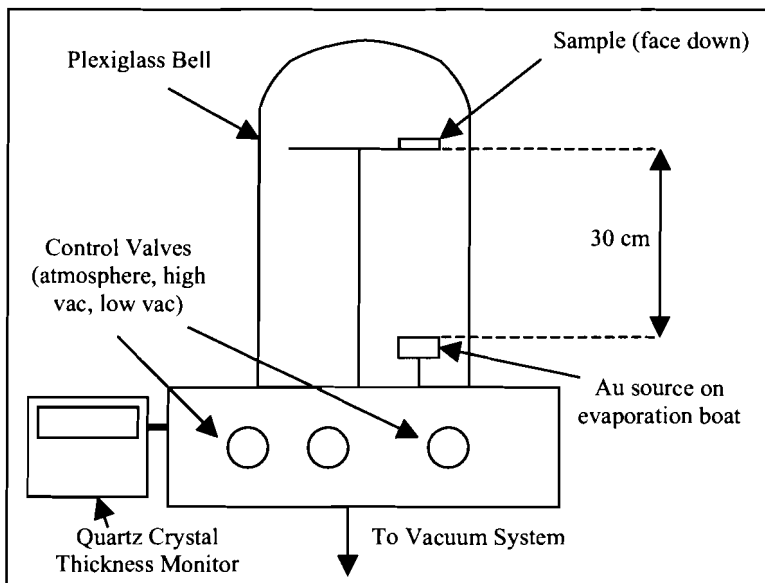


Figure 2-3 Schematic diagrams of the apparatus used to deposit gold pads onto silicon wafer.

Figure 2-3 depicts the apparatus used to deposit gold onto the surface, consisting of a vacuum chamber made of a steel base covered with a Plexiglas bell, containing the sample holder, resistive heating element, and valves connecting to a vacuum pump. The first step is placing an evaporation mask over the surface of the sample. The mask has nine holes, each 3 mm in diameter, drilled into an aluminium block (30×20×5 mm); it is placed directly on the surface of the wafer, with Teflon tape acting as a spacer. The purpose of the mask is to create discrete devices. The sample with evaporation mask is then placed face down on a rotating sample holder on top of an evaporation shield, positioned 30 cm above the resistive heating element, which is constructed of aluminium and coated with aluminium oxide; it contains a small amount of 99.999% gold. After applying high-vacuum grease to the surface of the rubber seal on the Plexiglas bell, the

two sections of the chamber are connected and the chamber is evacuated. When the pressure reaches 10^{-5} Torr and the shield is still blocking the path from the evaporation boat to the sample, a current is applied to the resistive boat and the gold is melted to ensure that there is no organic contamination on its surface before deposition. When the pressure stabilizes again, the sample is rotated to a position directly above the gold, where the evaporation shield is no longer blocking the path to the sample, and 10 nm of gold is deposited onto the surface at a rate of 0.1 nm/s. The sample is then removed from the chamber and is ready for analysis.

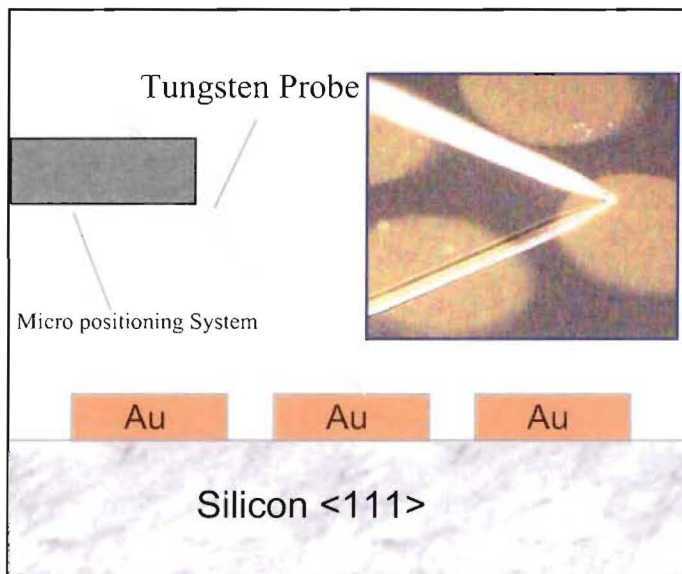


Figure 2-4 Schematic diagram of the gold pad *J-V* probe apparatus. The inset shows an optical image of the probe contacting a 3-mm diameter gold pad on the surface of a C10-Si sample.

2.3 Instrumentation

Atomic Force Microscope (AFM) images were obtained using a Topometrix Explorer AFM (2 μm -Z-linearized scanner) using silicon nitride tips (triangular D of MSCT-AUHW, Veeco Metrology group, resonance frequency 15 kHz, force constant 0.03 N/m). Images were acquired in contact mode and analyzed using Thermomicroscopes SPM Lab Software. Modified silicon wafers were placed into the AFM sample holder and held in place with several clamps. AFM tips were carefully brought into contact and let sit for several hours before scans were performed.

Attenuated Total Reflectance-Fourier-Transform Infrared (ATR-FTIR) spectra were recorded using a ThermoNicolet Nexus-IR 560 spectrometer equipped with a mercury cadmium telluride (MCT) detector cooled with liquid nitrogen. ATR crystals (double-side polished un-doped silicon; 25 \times 5 \times 1 mm with 45° bevels at either end, Harrick Scientific, Inc.), modified via the same procedures used to modify silicon wafers for electrical measurements, were mounted into the chamber, the IR beam focused onto one of the bevels, and the chamber was then purged with a continuous stream of dry air for an hour before spectra collection. Background spectra consisting of hydrogen-terminated silicon surfaces were subtracted from the organically modified silicon IR spectra. All spectra were obtained from an overlay of 1000 scans taken with 2 cm^{-1} resolutions between wavenumbers 1500 and 4000 cm^{-1} . No corrections for atmospheric water vapour or CO₂ were performed. Minimal baseline correction was applied to subtracted spectra.

Wetting measurements were carried out using a VCA Optima (AST Products, Inc.) system in ambient conditions (19-23 °C, 30-35% relative humidity). The modified silicon wafer was placed onto the level stage of the apparatus. A 2- μ L droplet of water was then deposited onto the sample wafer with a micropipette. Next, a picture of the cross-section of the horizontally illuminated water droplet on the surface of the wafer was taken. Five points on the image of the droplet were selected and a curve was automatically fit, from which the angle that the water droplet forms with the surface was extracted. Five independent measurements were made for each sample, always using a fresh water droplet.

Macroscale Electrical Measurements The current density-voltage (J - V) measurements with mercury drop contacts were carried out with an Autolab Electrochemical Analyzer (Model: PGSTAT30, Eco Chemie BV, Netherlands). Bottom InGa and top mercury drop contacts were formed to the modified silicon wafer inside a Faraday cage, which was closed during measurements to prevent both room-light illumination (photoluminescence) and electrical noise (which can interfere with the measured signal). An optical image of the mercury droplet on the surface of the sample was taken in order to determine the electrode contact area. A linear J - V scan was performed from -0.5 V (forward bias, silicon is the cathode) to +0.5 V (reverse bias, silicon is the anode) with a step size of 0.007 V and at a scan rate of 0.05 Vs⁻¹. A new top contact was then formed on a different part of the sample and another scan performed; this was repeated between 4 and 7 times per sample. There was no observed breakdown of the junctions within the measured voltage range for any J - V scans.

Mott-Schottky (*M-S*) measurements were performed using the same instrumental set-up as with the mercury drop *J-V* measurements. *M-S* measurements were collected at a frequency of 1MHz from – 0.2 V to + 1.0 V with step potentials of 0.1 V.

The *J-V* measurements on thermally deposited gold pads were carried out with the same Electrochemical Analyzer. After a gold pad was deposited on the surface of the monolayer-modified silicon wafer through an evaporation mask, a back contact was formed using an indium-gallium eutectic, and the sample was placed in a Faraday cage. The gold pad was connected to the circuit by lowering a sharpened tungsten tip onto the surface with a micro-positioning system. Contact was determined by monitoring the potentiostat, which reads 0 V only when the circuit is complete (no voltage is yet applied). The Faraday cage is then closed to prevent both room-light illumination (photocurrent) and electrical noise (which can interfere with the measured signal), then a linear scan was performed from -1.0 V (forward bias, silicon is the cathode) to +1.0 V (reverse bias, silicon is the anode) with a step size of 0.007 V and at a scan rate of 0.05 Vs⁻¹. The tungsten tip was then repositioned on a different gold pad and another scan was performed; this was repeated between 4 and 7 times per sample. There was no observed breakdown of the junctions within the measured voltage range for any *J-V* scans. Mott-Schottky measurements were collected at 1MHz from – 0.2 V to + 1.0 V with step potentials of 0.1 V.

Scanning Tunneling Microscopy/Ballistic Electron Emission Microscopy (STM/BEEM) STM/BEEM measurements were performed using a custom-built BEEM amplifier connected to a commercial Omicron STM1 STM. A back electrical contact connecting the sample to the BEEM circuit was formed by scoring the backside of the

silicon wafer with a diamond-coated pen and applying an InGa eutectic. The sample was then held in place with a Teflon clip. Thermally evaporated gold pads were used as the top electrical contact, which was connected to the STM tunneling circuit using a tungsten tip. The metal contact is directly grounded while the semiconductor is grounded through a virtual ground of the BEEM operational amplifier. Bias is applied only between the STM tip and the metal contact.

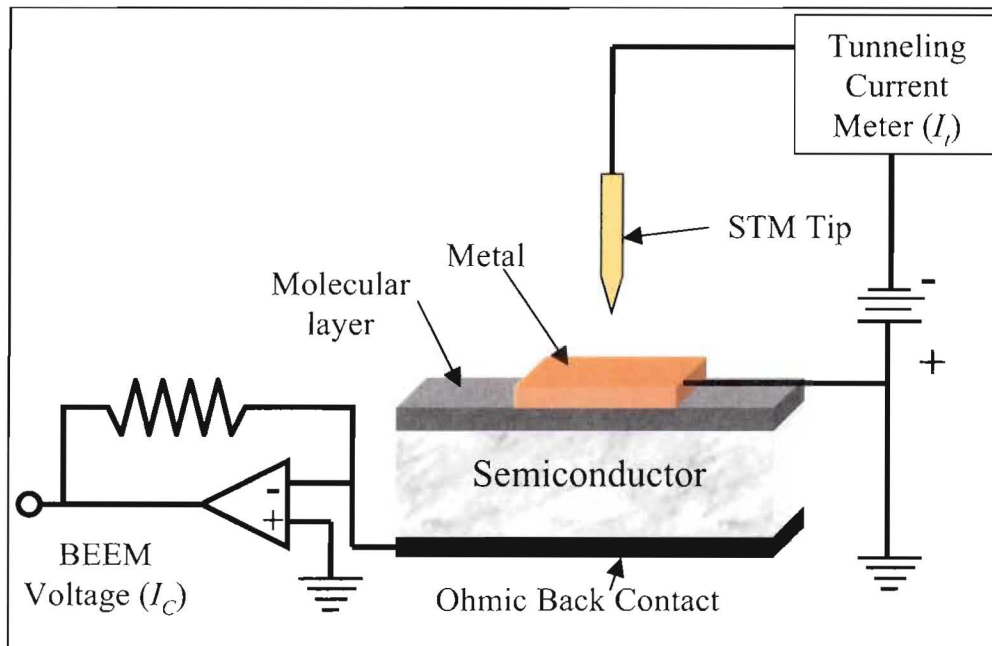


Figure 2-5 Schematic diagram of a ballistic electron emission microscope.

Two types of imaging were performed, two-dimensional spatial imaging and static BEEM $I-V$ measurements. In the two-dimensional spatial imaging mode, a feedback loop maintains a constant voltage and current between the STM tip and the sample while the STM-height piezo potential and BEEM collector-current were recorded, giving simultaneous topographic STM and BEEM current images respectively. In the BEEM $I-V$ mode, the STM tip is positioned at a desired location on the sample and the

BEEM collector current (I_c) is recorded as a function of the applied STM tip bias (V_t) while maintaining a constant tunneling current.

In both modes, there is no bias applied between the metal and the semiconductor other than a small fixed (mV) bias resulting from the high-gain BEEM op-amp circuit. The tip is negatively biased with respect to a grounded metal layer, meaning transport occurs in the direction of STM tip (Pt:Ir; 90:10 wt%) to metal and semiconductor. The BEEM voltage threshold, which for each spectrum in this work, was extracted by a theoretical fit based on the Bell-Kaiser model³⁷.

Transmission Electron Microscopy TEM studies were carried out using a field-emission source operating at 200 kV. TEM samples were prepared by mechanical thinning at room temperature, followed by Ar ion milling (5 kV, 5 μ A) with liquid nitrogen cooling.

2.4 Data Analysis

2.4.1 Macroscale J - V Measurements

The major transport mechanism for charge carriers across semiconductor-insulator-metal diodes is a thermionic emission process whereby the electrons or holes tunnel through the insulator. Using thermionic emission theory, we can obtain a quantitative comparison of monolayer effects by using the following equation¹³:

$$J = A^* T^2 e^{(-\beta l)} e^{-(q\phi_b/kT)} e^{(qV/nkT)} [1 - e^{(-qV/kT)}] \quad \text{Equation 2.1}$$

where J is the measured current density in $\text{A}\cdot\text{cm}^{-2}$, V is the applied bias voltage in V , A^* is the Richardson constant ($110 \text{ AK}^{-2}\text{cm}^{-2}$), q is the electronic charge, l the thickness of

the monolayer, T the absolute temperature in K, and k is Boltzmann's constant. The term n is the ideality factor where $n = 1$ for an ideal diode and $n > 1$ for diodes where the charge carrier transport mechanism is not exclusively due to thermionic emission. The term ϕ_b is the potential barrier height encountered by electrons in the semiconductor alone, and $e^{(-\beta l)}$ is a structure-dependent attenuation factor, which depends on the tunnelling mechanism and describes the decrease in current density due to the monolayer.

The effective barrier height can then be defined as the barrier encountered by electrons in the metal passing to the semiconductor which is due to both the barrier in the semiconductor itself (caused by interface states) as well as the tunnelling barrier presented by molecules on the surface of the semiconductor³¹:

$$q\phi_{eff} = q\phi_b + kT\beta l \quad \text{Equation 2.2}$$

where $q\phi_b$ is the energy barrier due to the semiconductor and $kT\beta l$ is the tunnelling barrier presented by the molecules.

Equation 2.1 can then be re-arranged as:

$$J = A * T^2 e^{-(q\phi_{eff} / kT)} e^{(qV / nkT)} [1 - e^{(-qV / kT)}] \quad \text{Equation 2.3}$$

By plotting a graph of $\ln(\frac{J}{1 - e^{(-qV / kT)}})$ vs. V , we can extract the ideality factor n from the slope and $q\phi_{eff}$ from the intercept.

2.4.2 Macroscale C-V Measurements

Further information on the electrical properties of the constructed metal-monolayer-semiconductor junctions was gathered using capacitance measurements. The capacitance is defined as the total electric charge in a system divided by the potential across the system. In the case of thin insulators on a semiconductor, the capacitance in accumulation often does not reach a constant value. The capacitance is then considered a series circuit of the thin film insulator and the semiconductor. It is calculated as the sum of the insulator capacitance (C_{ins}) and the semiconductor capacitance (C_s) (Eq. 4.4¹³)

$$\frac{1}{C} = \frac{1}{C_{ins}} + \frac{1}{C_s} = \frac{1}{C_{ins}} - \frac{2kT}{qC_{ins}} \frac{1}{(V_{bias} - V_{fb} - \psi_s)} \approx \frac{1}{C_{ins}} - \frac{2kT}{qC_{ins}} \frac{1}{(V_{bias} - V_{fb})} \quad \text{Equation 2.4}$$

However, due to the capacitance in accumulation not reaching a constant value, C-V plots appear distorted. In these cases, important electrical parameters such as the built-in potential (V_{do} , surface potential at zero bias) can be extracted using the Mott-Schottky method. With this method, the potential drop across the insulator is considered negligible compared to the potential drop in the semiconductor depletion layer, and the capacitance per unit area can be expressed by¹³:

$$\frac{1}{C^2} = \frac{2(V_{do} - V)}{\varepsilon_s \varepsilon_o N_d q} \quad \text{Equation 2.5}$$

where C is the depletion layer capacitance per unit area, V is the applied potential, V_{do} is the built-in potential, N_d is the dopant density, ε_s is the relative permittivity (dielectric constant) of the semiconductor, and ε_o is the permittivity of free space. By plotting the Mott-Schottky data (C^2 vs. V), the dopant density can be extracted from the slope, and

the surface potential can be extracted from the intercept of the linear portion of the Mott-Schottky plot at reverse bias.

The barrier height can then be calculated from¹³:

$$\phi_b = V_{do} + V_n = V_{do} + (kT/q) \ln(N_c / N_d) \quad \text{Equation 2.6}$$

where V_n is the energy difference between the Fermi level and the conduction band in the bulk semiconductor, and N_c is the carrier density in the conduction band of the semiconductor ($N_c = 2.78 \times 10^{19} \text{ cm}^{-3}$ for silicon).

2.4.3 Ballistic Electron Emission Microscopy

One of the goals in the study of molecular electronic systems has been the reliable, reproducible measurement of the electrical properties at the molecular scale, both for producing functional single-molecule devices as well as for studying behaviour that may be unique at such scales. Conventional instrumental measurements such as mercury drop and gold pad $J-V$ are unable to provide such information despite providing valuable information on the average electrical behaviour of the device. At the large scale of the contacts, small regions with the lowest barrier heights will dominate the observed electrical characteristics.

One technique that can provide ~ 10 -nanometer resolution is ballistic electron emission microscopy (BEEM)³⁸⁻⁴⁰. In this device set-up, a scanning tunnelling microscope (STM) is used to inject electrons, of an energy determined by the tip-sample bias, into a thin metallic film that forms the top contact of a metal-molecule-semiconductor device. If the electrons have sufficient energy, and the metal thickness is less than the mean free path of the electrons (< 10 nm for gold), a small fraction of them

will be able to reach the interface and cross the Schottky barrier without scattering and be collected at the back electrical contact as BEEM current. Because only ballistic electrons emitted over the Schottky barrier are measured, there are no contributions from other, parasitic current mechanisms which could significantly dominate conventional I - V characteristics⁴¹.

The Bell-Kaiser model for ballistic electron transmission⁴² allows the fitting of BEEM I - V spectra in order to extract the threshold voltage, V_b , which is the potential at which the barrier to electron transfer from the semiconductor to the metal is 0.

In the Bell-Kaiser model, the tunneling current, I_t , between the STM tip and the gold contact can be calculated using equation:

$$I_t = C \int_0^{\infty} D(E_x) 0 \int_0^{\infty} [f(E) - f(E + eV)] dE_i dE_x \quad \text{Equation 2.7}$$

where $D(E_x)$ is the transmission probability for an electron to tunnel through the vacuum barrier, $f(E)$ is the Fermi function, and C is a constant.

The collector current, I_c , for the BEEM circuit is defined as:

$$I_c = RC \int_{E_{\min}}^{\infty} D(E_x) \int_0^{E_{\max}} f(E) dE_i dE_x \quad \text{Equation 2.8}$$

where R is a measure of attenuation due to scattering in the base layer.

By combining equations 2.7 and 2.8 the collector current in terms of the tunneling current can be extracted:

$$I_c = RI_t \frac{\int\limits_{E_{\min}}^{\infty} D(E_x) \int\limits_0^{E_{\max}} f(E) dE_t dE_x}{\int\limits_0^{\infty} D(E_x) \int\limits_0^{\infty} [f(E) - f(E + eV)] dE_t dE_x}$$

Equation 2.9

Equation 2.9 predicts that the I - V spectra for metal-semiconductor diodes behave as $(V - V_b)^2$ for voltages just above the threshold value.

CHAPTER 3: STRUCTURAL AND SPECTROSCOPIC CHARACTERIZATION OF ORGANIC MONOLAYERS ON SILICON

Prior to the electrical characterization of monolayer-modified silicon, it was necessary to determine the composition and quality of the monolayers. Therefore, the silicon samples were characterized using the techniques of atomic force microscopy (AFM), contact angle measurements, and infrared spectroscopy (FT-IR).

3.1 Atomic Force Microscopy

AFM is a type of scanning probe microscope that detects the vertical deflection of a cantilever as it is scanned across the surface of a sample. The deflection is directly correlated to the topographical features of the surface and can be used to determine the roughness of a sample, as well as detect any surface features such as attached nanoparticles.

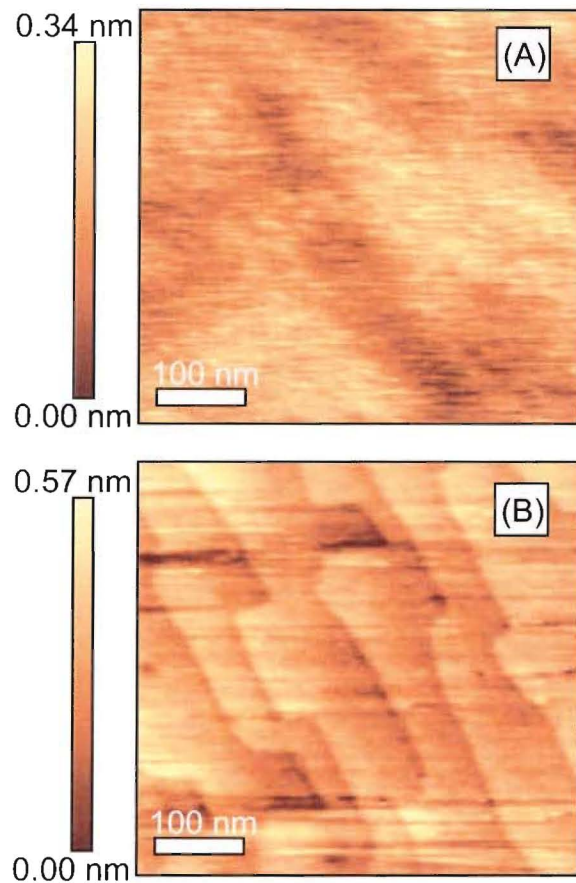


Figure 3-1 Contact mode AFM image of (A) $\text{SiO}_2\text{-Si}$ and (B) C10-Si.

Figure 3-1 shows a typical AFM image of an oxidized silicon (A) and a surface modified with 1-decyl monolayers (B). The most notable difference between the two samples is the significantly greater roughness of the oxide sample compared to the monolayer-modified sample, demonstrating the fact that the monolayer is protecting the silicon surface from oxidation. Steps corresponding to the inter-atomic separation of silicon atoms in the crystal are visible for C10-Si while no discernable features are visible for the oxide sample. While the molecules themselves cannot be resolved in this image, the topography consists of a series of terraces approximately 100 nm wide with

approximately 0.23-nm steps. This particular surface structure is characteristic of a single monolayer on the surface of the silicon (111) wafer. The topography imaged here reflects that of the underlying substrate, with the molecular layer conforming perfectly to the surface.

3.2 ATR/FT-IR

Attenuated Total Reflectance – Fourier Transform Infrared Spectroscopy (ATR-FTIR) is a type of infrared spectroscopy whereby an IR beam is projected at an angle to the surface of an ATR crystal covered with a monolayer of interest. For silicon ATR crystals, for which the refractive index of silicon is 3.875, an angle of 45° is used, which results in both total internal reflection as well as the formation of an evanescent wave. An evanescent wave is an electromagnetic field that projects perpendicularly into the surface of the crystal when the IR beam is reflected at an angle greater than the critical angle.

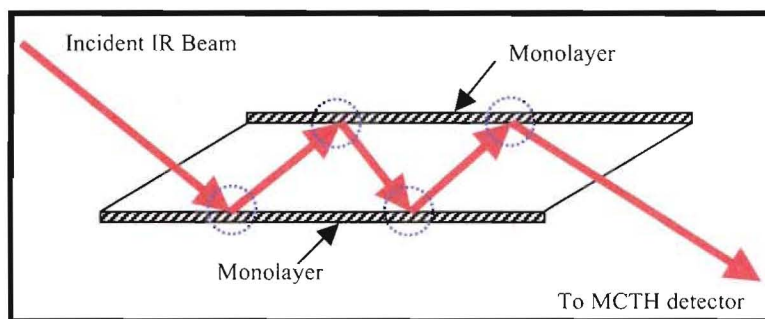


Figure 3-2 Diagram of an ATR crystal with an IR beam (red arrows) undergoing multiple internal reflections.

Every time the IR beam is internally reflected from the crystal surface, an evanescent wave is produced. The intensity of this evanescent wave decreases

exponentially with distance from the surface, with the decay length, δ , being a function of the refractive indices (n_1 and n_2) and the critical angle (θ_{crit}):

$$\delta = \frac{\lambda}{2\pi(\sqrt{n_1^2 \sin 2\theta_{crit}} - n_2^2)} \quad \text{Equation 3.1}$$

The monolayers attached to the surface of the silicon crystal can therefore be probed by these evanescent waves and an absorbance spectrum of the monolayer can be collected. ATR crystals of polygonal structure composed of undoped silicon (111) were modified by the same procedure as with n-silicon (111) wafers. First, an H-Si background was obtained, and then a modified ATR crystal was scanned. After matching the sample backgrounds (to account for moisture), an IR spectrum was obtained.

The major IR bands used for the characterization of the molecules attached to silicon were the symmetric and asymmetric CH_2 peaks ($\nu_s\text{CH}_2$ and $\nu_a\text{CH}_2$, respectively), and the asymmetric CH_3 peak ($\nu_a\text{CH}_3$). In the case of silicon modified with thioacetate functionalised alkanes (AcSC11-Si), the C=O stretching mode was used. Additionally, negative absorbance due to the Si-H background and differences in atmospheric CO_2 are observed at 2080 cm^{-1} and 2350 cm^{-1} , respectively.

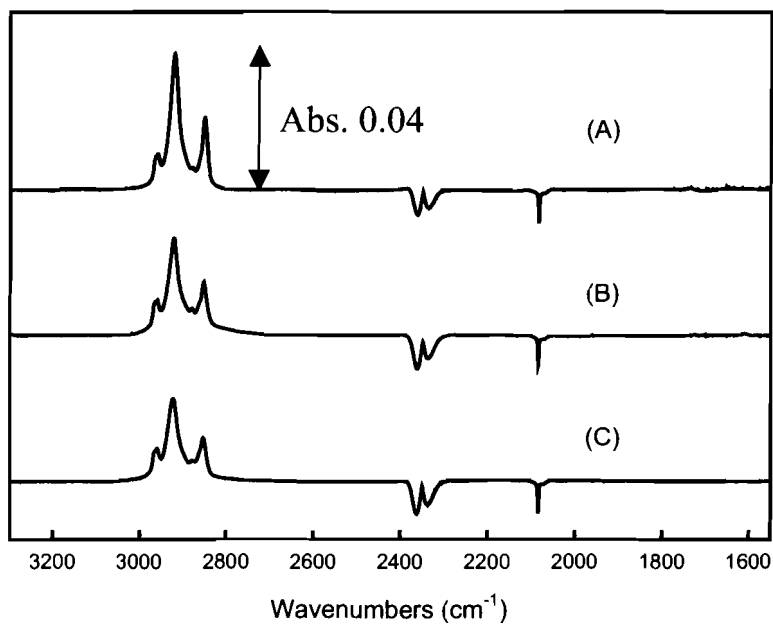


Figure 3-2 ATR-FTIR spectra of (A) C12-Si, (B) C10-Si, and (C) C8-Si samples.

Table 3-1 FT-IR data for Silicon modified with organic monolayers.

Sample	$\nu_a\text{CH}_3(\text{cm}^{-1})$	$\nu_a\text{CH}_2(\text{cm}^{-1})$	$\nu_s\text{CH}_2(\text{cm}^{-1})$	$\nu\text{C=O}(\text{cm}^{-1})$
C6-Si	2959	2925	2860	---
C8-Si	2959	2923	2853	---
C10-Si	2960	2921	2852	---
C12-Si	2960	2920	2852	---
AcSC11-Si	---	2925	2855	1698
HSC11-Si	---	2927	2855	---

Figure 3-2 shows typical IR spectra of n-alkyl monolayers on silicon; the peak assignments and positions are listed in Table 3-1. All of these samples (C8-Si, C10-Si, and C12-Si) exhibit $\nu_s\text{CH}_2$ and $\nu_a\text{CH}_2$ peaks at the frequencies of 2853 cm^{-1} and

2923 cm^{-1} , respectively, which is consistent with literature data for these systems.¹ The $\nu_{\text{a}}\text{CH}_3$ stretching mode is also present at 2959 cm^{-1} . Also of note is the fact that the intensities of the peaks increase with increasing chain length. This is due to a combination of longer alkyl monolayers having a greater number of CH_2 groups as well as a possible increase in the surface density of the molecules.

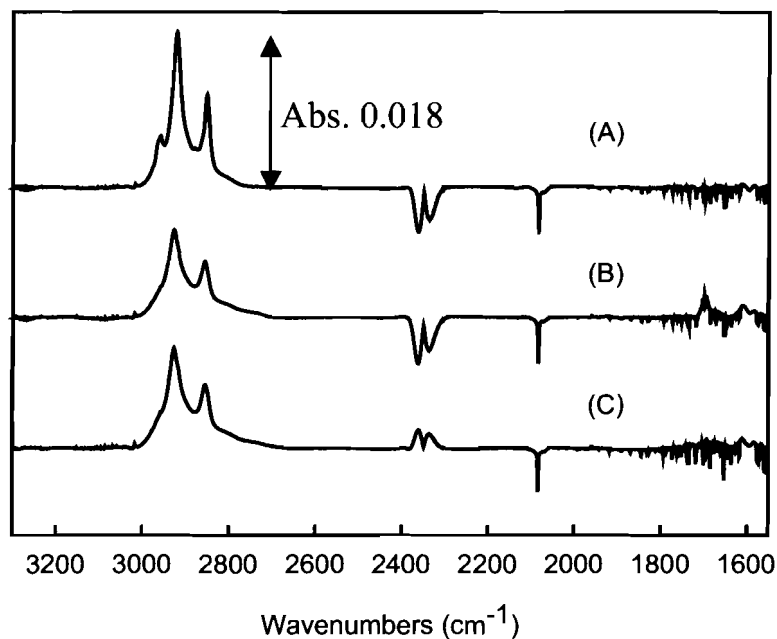


Figure 3-3 ATR-FTIR spectra for (A) C12T-Si , (B) AcSC11-Si , and (C) HSC11-Si .

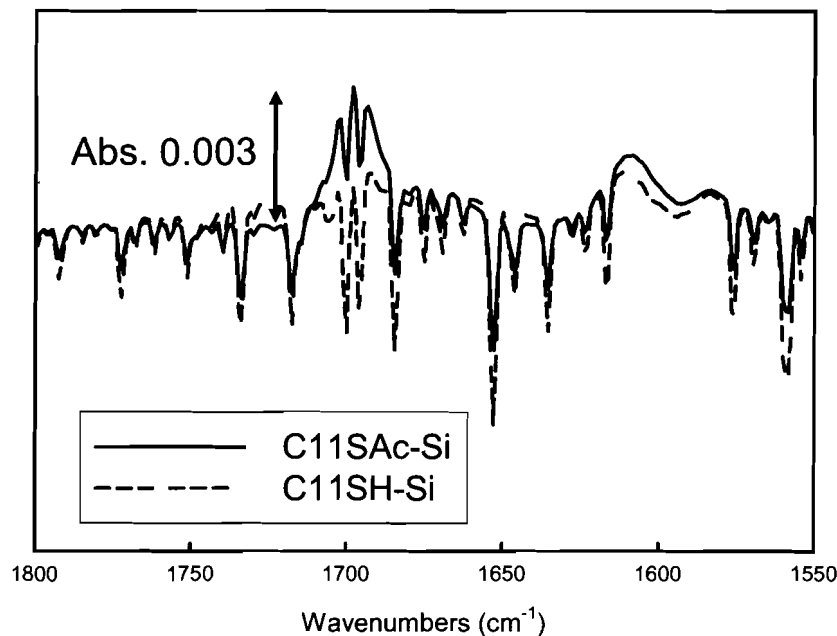


Figure 3-4 FT-IR overlay of AcSC11-Si (solid line) and HSC11-Si (dashed line) highlighting the loss of carbonyl absorption upon deprotection of AcSC11-Si.

For the AcSC11-Si and HSC11-Si samples (Figures 3-3), we see again the $\nu_s\text{CH}_2$ and $\nu_a\text{CH}_2$ peaks at 2855 cm⁻¹ and 2925 cm⁻¹, respectively. The $\nu_a\text{CH}_3$ peak, which we would expect to see in the AcSC11-Si sample, however, is not as readily visible as with n-alkyl monolayers. This may be a result of a change in the chemical environment at the terminal end of the monolayer. While in the C12_T-Si sample the entire chain consists of CH₂ groups with methyl termination, the AcSC11-Si sample also has CH₂ groups adjacent to—C(O)S- groups. The electron-withdrawing properties of the thioacetate group result in a broadening of the CH₂ stretching frequency range. This broadened $\nu_s\text{CH}_2$ overlaps with the $\nu_a\text{CH}_3$ frequency, masking the latter signal.

In addition to the $\nu_s\text{CH}_2$, $\nu_a\text{CH}_2$ and $\nu_a\text{CH}_3$ peaks, AcSC11-Si also had absorption at 1698 cm⁻¹, which corresponds to a C=O stretching mode of the terminal thioacetate

group. Upon deprotecting the AcSC11-Si sample to yield HSC11-Si, the only change observed in the IR spectrum is the loss of the C=O peak (Figure 3-4), which can be used as an indicator of deprotection. The S-H IR stretching frequency (2600-2550 cm⁻¹) cannot be detected as it's intensity is very weak.⁴³

3.3 Wetting Measurements

Wetting measurements are methods by which the relative hydrophobicity / hydrophilicity of a surface can be determined. Several parameters, both chemical and structural, can affect the measured contact angles. The functional groups of the monolayer that are exposed to the water droplet can increase or decrease the measured contact angle with increasing or decreasing polarity, respectively. The order of monolayer packing and the density of packing can also affect the surface hydrophobicity, with rougher surfaces giving higher water droplet contact angles.

Table 3-2 Contact angles made with 2- μ L droplets of de-ionized water on surfaces of SiO₂-Si, H-Si, C6-Si, C8-Si, C10-Si, C12-Si, AcSC11-Si, and HSC11-Si.

Sample	Contact Angle (°)
SiO ₂ -Si	23 ± 4
H-Si	82 ± 6
C6-Si	97 ± 2
C8-Si	106 ± 1
C10-Si	106 ± 3
C12-Si	107 ± 2
AcSC11-Si	81 ± 9
HSC11-Si	72 ± 2

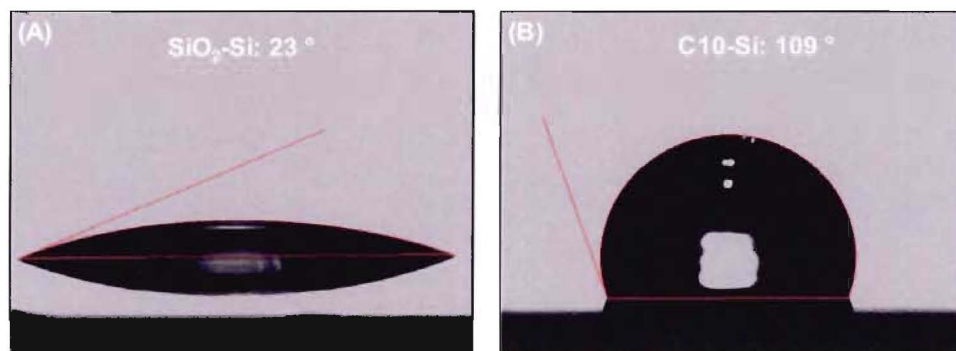


Figure 3-5 Cross-sectional optical images of a typical (A) hydrophilic SiO₂-Si and (B) a hydrophobic C10-Si wafer.

Table 3-2 lists the contact angles obtained for bare, oxidized, and molecularly modified silicon and Figure 3-5 shows representative cross sectional images used to calculate the contact angles. Oxidized silicon samples exhibited the lowest contact angle, due to the surface oxygen atoms to hydrogen bond to the water droplet. H-Si samples have a contact angle of $82 \pm 6^\circ$ due to their relatively hydrophobic nature. The alkyl

monolayer surfaces C8-Si, C10-Si and C12-Si all gave water contact angles of $106 \pm 2^\circ$. This value is consistent with a model of a well packed/ordered alkyl monolayer covalently linked to a silicon surface, with values consistent with literature data for the same system.⁴⁴ C6-Si shows a lower contact angle than C8-Si, C10-Si and C12-Si. This discrepancy is possibly a result of the shorter chain-length C6 monolayers having a lower monolayer surface density resulting in fewer hydrophobic methyl groups at the surface.

Contact angles for the AcSC11-Si samples were approximately 81° , a value consistent to within experimental error with literature data for similar monolayers formed via C-O-Si linkages.³⁶ The lower contact angle relative to alkyl chains of similar length is due to the presence of the terminal acetate functionality. Upon deprotection of AcSC11-Si to give HSC11-Si, we see a decrease in the contact angle to 72° . This value is also consistent with literature values on similar systems.³⁶ The decrease is once again attributable to the hydrophilicity of the terminal functionality.

CHAPTER 4: ELECTRICAL CHARACTERIZATION OF METAL-MONOLAYER-SEMICONDUCTOR JUNCTIONS

While techniques such as AFM, FT-IR and wetting measurements can provide a wealth of information about the structure and composition of a monolayer on the surface, they cannot predict the performance of metal | monolayer-semiconductor junctions. The reasons for this include the inability of these analytical methods to penetrate to the interface of the semiconductor, the averaging of junction properties due to the scale of measurements (i.e., size of IR beam $\sim 1000 \mu\text{m}$), and sensitivity. One solution is the use of current density-voltage ($J-V$) and capacitance-voltage ($C-V$) measurements to probe the electrical performance of these organic materials.

4.1 Electrical Characterization of Oxidized and Organically Modified Silicon Surfaces

One of the goals of the electronics industry has been, since inception, to exercise a greater degree of control over the insulating/passivating materials used with semiconductor devices. Currently, this role is primarily filled, in the case of silicon-based devices, with a thin layer of thermally grown oxide. Due to physical limitations of oxide materials and the drive to develop sensors where probes are directly incorporated onto the semiconductor surface, research into organic molecules as passivating/insulating layers on silicon has taken on a great interest. As it is our goal to understand the manner in which modifying a bare silicon surface with organic molecules affects their electrical properties, it is first necessary to carry out a comparison among the systems of un-

oxidised silicon, oxidised silicon and a representative organically modified silicon surface.

4.1.1 Macroscale Electrical Characterization

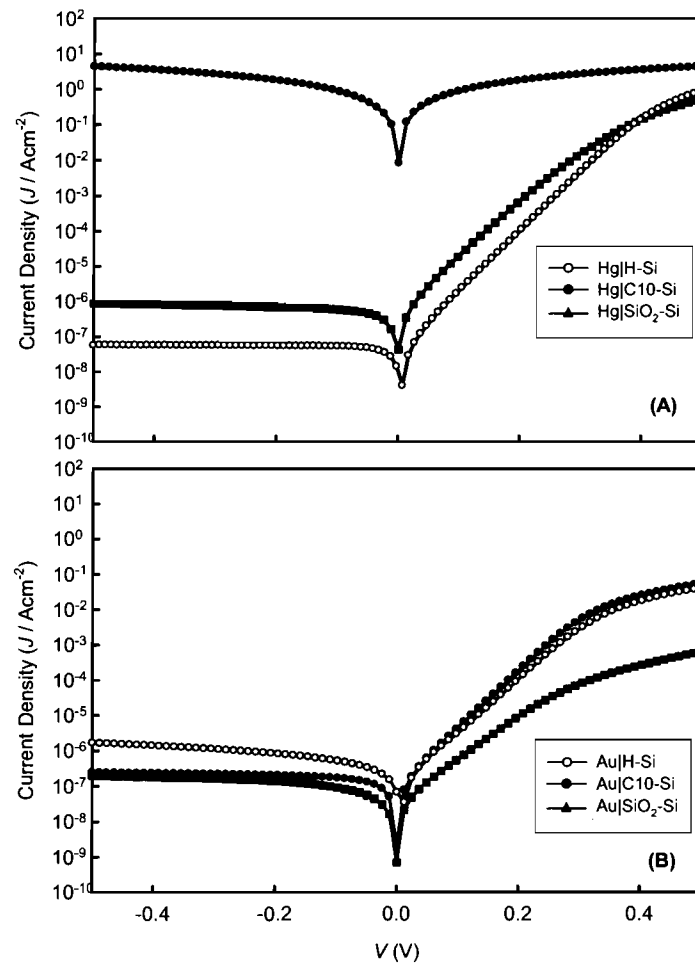


Figure 4-1 Logarithmic current density plots for H-Si, SiO₂-Si, and C10-Si surfaces as measured by (A) mercury drop and (B) gold pad top electrical contacts.

Table 4-1 Ideality factors (n) and barrier heights ($q\phi_{eff}$) for H-Si, C10-Si and SiO₂-Si as measured by mercury drop and gold pad electrical contacts.

Mercury Drop			Au Pad	
Sample	n	$q\phi_{eff}/\text{eV}$	n	$q\phi_{eff}/\text{eV}$
H-Si	Ohmic Contact	Ohmic Contact	1.05 ± 0.05	0.83 ± 0.01
C10-Si	1.17 ± 0.16	0.85 ± 0.04	1.14 ± 0.10	0.82 ± 0.01
SiO ₂ -Si	1.50 ± 0.36	0.75 ± 0.03	1.86 ± 0.10	0.82 ± 0.01

Figure 4-1 shows the typical J - V behaviour of oxide-free, oxidized, and molecularly modified silicon junctions as measured with mercury and gold electrodes. Hg|H-Si junctions displayed ohmic behaviour (symmetric with respect to zero bias), while Hg|SiO₂-Si and Hg|C10-Si junctions displayed rectifying behaviour (the current densities under forward bias, with respect to silicon, were significantly higher than those under reverse bias). This difference can be explained by equation 1.1, which correlates the barrier height with the work function of the metal and the electron affinity of the semiconductor. Using literature values for the work function of mercury⁴⁵ (4.53 ± 0.04 eV) and the electron affinity of n-doped silicon⁴⁶ (4.05 ± 0.08 eV), we would expect a barrier height of 0.48 eV. Because the electrical measurements are performed under ambient conditions (298 K), the electrons have sufficient energy to cross the barrier without significant impedance, resulting in an ohmic-like contact (no difference in forward and reverse bias).

For the Hg|SiO₂-Si and Hg|C10-Si junctions however, the introduction of an oxide or organic monolayer results in an additional tunnelling barrier (due to the insulator) over

the intrinsic barrier of the metal-semiconductor. This increased effective barrier height is sufficient to result in rectifying J - V characteristics for the junctions. The following ideality factors were extracted using the thermionic emission model with added tunnelling factor (equation 2.3): $n = 1.50 \pm 0.36$ and $q\phi_{eff} = 0.75 \pm 0.03$ eV for Hg|SiO₂-Si and $n = 1.17 \pm 0.16$ and $q\phi_{eff} = 0.85 \pm 0.04$ eV for Hg|C10-Si. These values are consistent to within experimental error with data from Liu et al.³² It can also be seen that while these junctions both showed rectifying current density – voltage behaviour, the current passing across a Hg|C10-Si was one order of magnitude lower than the Hg|SiO₂-Si junctions at any given bias below 0.4 V.

Junctions made with thermally evaporated gold as top electrical contact, (Au|H-Si, Au|SiO₂-Si, and Au|C10-Si) all resulted in rectifying J - V behaviour. The rectifying behaviour of the Au|H-Si junction (as opposed to the ohmic Hg|H-Si junction) is due to an increase in the work function of the metal (q_m) compared to Hg. For gold, q_m is 5.1 eV compared to 4.49 eV for Hg. The increase in work function would give a theoretical barrier height of 1.05 eV. The ideality factor and the barrier height of Au|H-Si junctions as measured with a gold top electrical contact were found to be $n = 1.05 \pm 0.05$ and $q\phi_{eff} = 0.83 \pm 0.01$ eV, respectively. While these values differ from the theoretically predicted values, it must be noted that the barrier of a metal|semiconductor junction may be dominated by the presence of interface states introduced by the extension of the wave function for the electrons of the metal into the energy gap of the semiconductor (MIGS). Accordingly, literature values for direct gold to n-silicon contacts are reported to be approximately 0.79 eV⁴⁷. The values obtained in our experiments are in agreement with these previous studies to within experimental error.

$\text{Au}|\text{SiO}_2\text{-Si}$ and $\text{Au}|\text{C10-Si}$ junctions also displayed rectifying behaviour, with comparable current density magnitude at a given applied bias. The extracted n and $q\phi_{\text{eff}}$ values were 1.86 ± 0.10 and 0.82 ± 0.01 eV for $\text{Au}|\text{SiO}_2\text{-Si}$, and 1.14 ± 0.17 and 0.83 ± 0.03 eV for $\text{Au}|\text{C10-Si}$. The reproducibility of the $\text{Au}|\text{SiO}_2\text{-Si}$ measurements, however, was lower than for the $\text{Au}|\text{C10-Si}$ junctions, as evidenced by the larger ideality factor (Table 4-1). Possible reasons are differences in the layer thickness, the intermixing of gold due to its initial surface impact and the migration of oxide to the top of the gold layer.

It is also of note that the $J-V$ behaviour of the $\text{Au}|\text{H-Si}$ and $\text{Au}|\text{C10-Si}$ junctions was almost identical. The lack of an increase in the barrier height on going from un-oxidized silicon to monolayer-passivated silicon when measuring $J-V$ behaviour with gold pads suggests that, in contrast to the $\text{Hg}|\text{C10-Si}$ junctions, there is no intervening molecular layer between the gold and the silicon; the deposited gold atoms are in fact penetrating into the monolayer and making a direct contact with the silicon surface. Due to the size of the metal contacts ($3000 \mu\text{m}$ for gold), the $\text{Au}|\text{H-Si}$ and $\text{Au}|\text{C10-Si}$ junctions cannot be distinguished, and the physical nature of the interface cannot be determined for certain, (i.e., whether the gold contacts the silicon by removing the monolayer or by penetrating into defects and gaps within the monolayer).

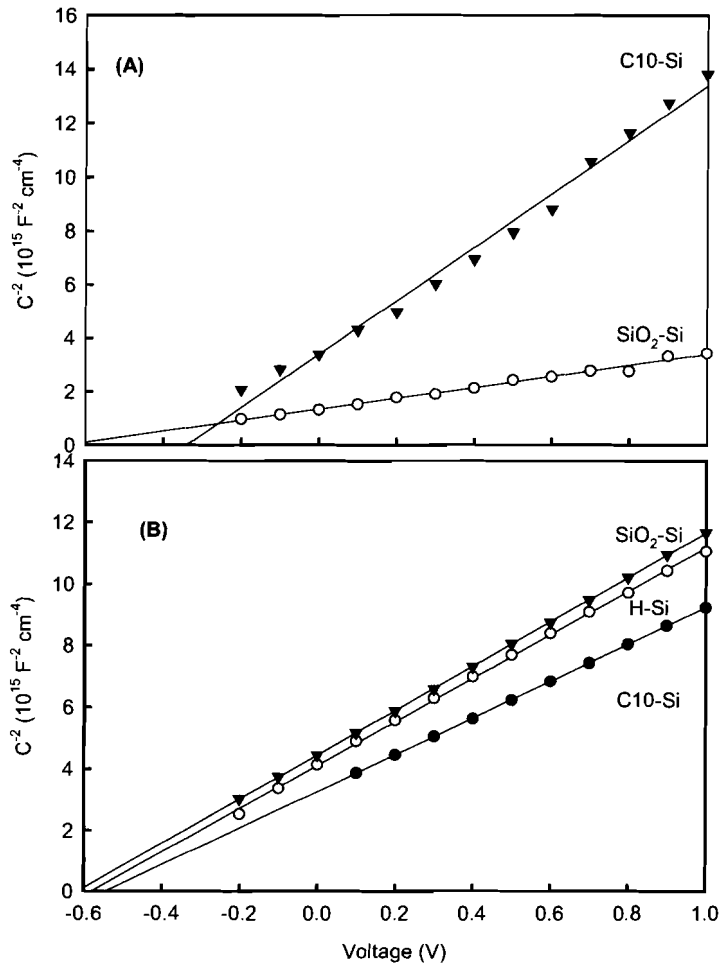


Figure 4-2 Mott-Schottky plots depicting the behaviour of H-Si, SiO₂-Si and C10-Si surfaces as measured by mercury drop (A) and gold pad (B) top electrical contacts.

Table 4-2 The calculated dopant density (N_d), built-in potential (V_{do}) and barrier height ($q\phi_b$) for H-Si, SiO₂-Si and C10-Si samples as measured by mercury drop and gold pad top electrical contacts.

Sample	Mercury Drop			Gold Pad		
	$N_d / \times 10^{15} \text{ cm}^{-3}$	V_{do} / V	$q\phi_b / \text{eV}$	$N_d / \times 10^{15} \text{ cm}^{-3}$	V_{do} / V	$q\phi_b / \text{eV}$
H-Si	---	---	---	1.7 ± 0.4	0.63 ± 0.11	0.83 ± 0.01
C10-Si	0.63 ± 0.22	0.35 ± 0.07	0.63 ± 0.07	2.1 ± 0.1	0.55 ± 0.03	0.79 ± 0.02
SiO ₂ -Si	0.93 ± 0.23	0.49 ± 0.08	0.69 ± 0.08	1.7 ± 0.1	0.62 ± 0.01	0.87 ± 0.01

In an ideal metal-insulator-semiconductor system, one in which the structure of the semiconductor surface is not changed by the introduction of an insulator, the $q\phi_b$ for modified samples would be expected to be equal to that for H-Si. Furthermore, in the case of H-Si, because there is no insulating layer between the metal and the semiconductor, there should be no contribution to the barrier from any insulating layer; hence the barrier height should be of the same magnitude as found with $J-V$ measurements. In Figure 4-2 we see the Mott-Schottky behaviour of the H-Si, SiO₂-Si, and C10-Si samples, with calculated values for V_{do} and $q\phi_b$ given in table 4-2. Among the mercury contact values, we see $q\phi_b$ values of 0.63 and 0.69 eV for C10-Si and SiO₂-Si, respectively, which is consistent with literature values³². Both values are lower than those obtained from mercury $J-V$ measurements, and also similar to the value obtained from $M-S$ measurements of the Hg|H-Si sample. The reason for this is that the barrier height extracted by the Mott-Schottky method does not include any contribution from the insulating layer. Therefore, we would expect all samples to have the same barrier height as does bare silicon, regardless of the insulator.

As expected, gold $M-S$ measurements gave similar values for the barrier heights of H-Si, C10-Si and SiO₂-Si: 0.83, 0.79 and 0.87 eV, respectively. In contrast to the mercury $M-S$ measurements, however, these values were almost identical to those calculated from gold $J-V$ measurements. This would indicate that there is widespread penetration of the gold into the molecular layer, and no contribution from the insulator. The difference in the magnitude of the barrier heights calculated from $M-S$ measurements with mercury and gold electrodes can also be attributed to the different work functions of gold and mercury.

4.1.2 Nanoscale Electrical Characterization

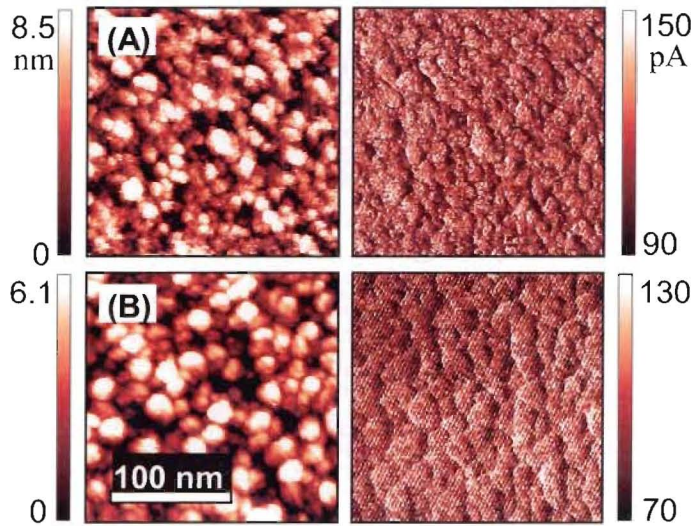


Figure 4-3 STM topography and corresponding BEEM current images for (A) Au|H-Si and (B) Au|C10-Si.

Figure 4-3 shows the STM topography and the corresponding BEEM current images for Au|H-Si and Au|C10-Si junctions obtained simultaneously at a tip bias $V_t = -2.0$ V and tip current $I_t = 4$ nA, with a scan area of 200×200 nm 2 . Due to the fact that no potential is applied across the junction during BEEM imaging, and SiO₂-Si samples present a barrier to ballistic electron transmission, no BEEM currents were obtained for the SiO₂-Si samples.

The STM images show the characteristic granular structure of thermally deposited gold films. Their corresponding BEEM current images show a strong correlation with the STM tunnelling images. Because a thicker gold film results in more electrons being scattered before reaching the interface, resulting in a lower BEEM current, the lateral variation in the BEEM current image is attributable to variations in the thickness of the gold film for both the Au|H-Si and Au|C10-Si junctions.

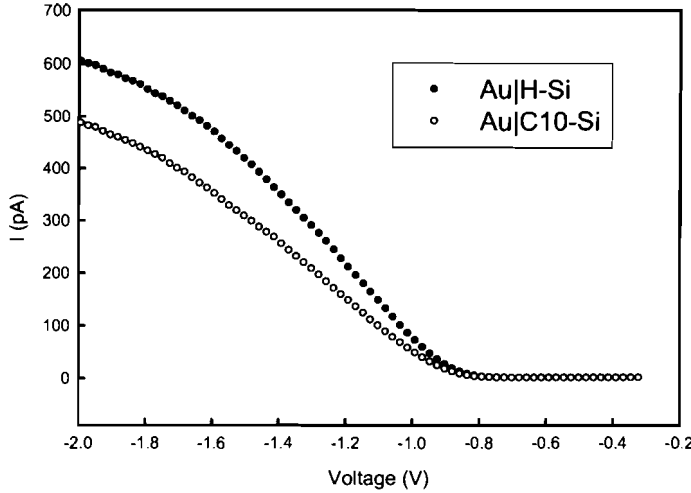


Figure 4-4 Static BEEM I - V curves for Au|H-Si and Au|C10-Si samples demonstrating a 20% decrease in BEEM current for C10-Si samples.

The averaged BEEM I - V spectra for Au|H-Si and Au|C10-Si junctions are shown in figure 4-4. Both samples had an identical average barrier thresholds of -0.82 ± 0.02 V (calculated using B-K model) which is consistent with previous results for direct Au|Si junctions^{48, 49}. The magnitude of the BEEM current for Au|C10-Si at a given potential is $\sim 20\%$ less than that of the Au|H-Si junction.

These nanoscale measurements demonstrate that for Au|C10-Si junctions, the interfacial monolayer did not contribute detectable lateral variations in the BEEM current. The surface coverage of n-alkyl monolayers on silicon is thought to be below 50% as a result of the 2×1 configuration for the alkyl chains attached to silicon (111)³⁵. Large ordered domains are also not expected to form because of the covalent bonding between adsorbates and substrate and the large lattice mismatch between silicon and alkyl monolayers. As a result, there is likely penetration of the monolayer by the thermally deposited gold atoms. The reduced BEEM current magnitude on going from bare silicon

to C10 protected silicon, however, indicates that even after thermal deposition of gold, molecules still remain present at the interface.

4.2 Electrical Properties of Metal|Monolayer-Silicon Junctions: Chain Length Dependence.

The tuneability of the electrical properties of molecularly modified silicon is one of the ultimate goals of molecular electronics. One of the simplest methods to examine its feasibility is to measure the electrical properties of silicon surfaces modified with a series of alkyl groups of increasing chain length. The increase in the chain length should result in an increased tunnelling barrier leading to an increased effective barrier height for the diode junction.

4.2.1 Macroscale Electrical Characterization

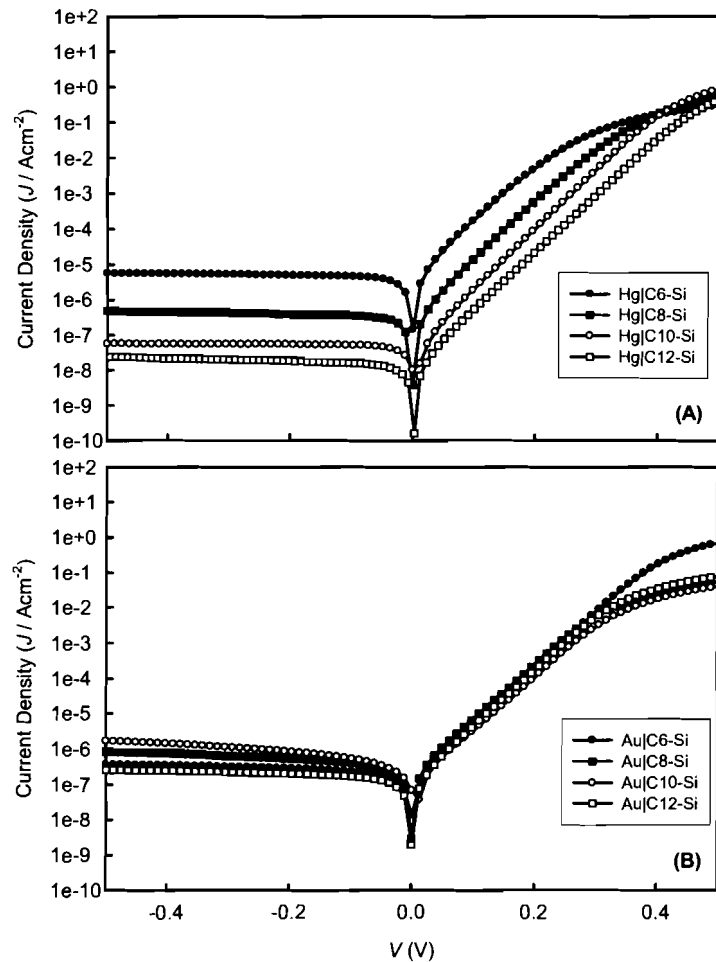


Figure 4-5 Log current density vs. voltage of a series of n-alkyl-modified silicon surfaces (C6-Si, C8-Si, C10-Si, C12-Si) as measured by mercury drop (A) and gold pad (B) top electrical contacts.

Table 4-3 Ideality factors (n) and barrier heights ($q\phi_{eff}$) for C6-Si, C8-Si, C10-Si and C12-Si as measured by mercury drop and gold pad top electrical contacts.

Sample	Mercury Drop		Gold Pad	
	n	$q\phi_{eff}/ \text{eV}$	n	$q\phi_{eff}/ \text{eV}$
C6-Si	1.11 ± 0.10	0.75 ± 0.03	1.07 ± 0.06	0.82 ± 0.01
C8-Si	1.13 ± 0.14	0.79 ± 0.03	1.08 ± 0.08	0.82 ± 0.02
C10-Si	1.17 ± 0.16	0.86 ± 0.04	1.14 ± 0.10	0.82 ± 0.01
C12-Si	1.34 ± 0.16	0.87 ± 0.02	1.05 ± 0.03	0.82 ± 0.03

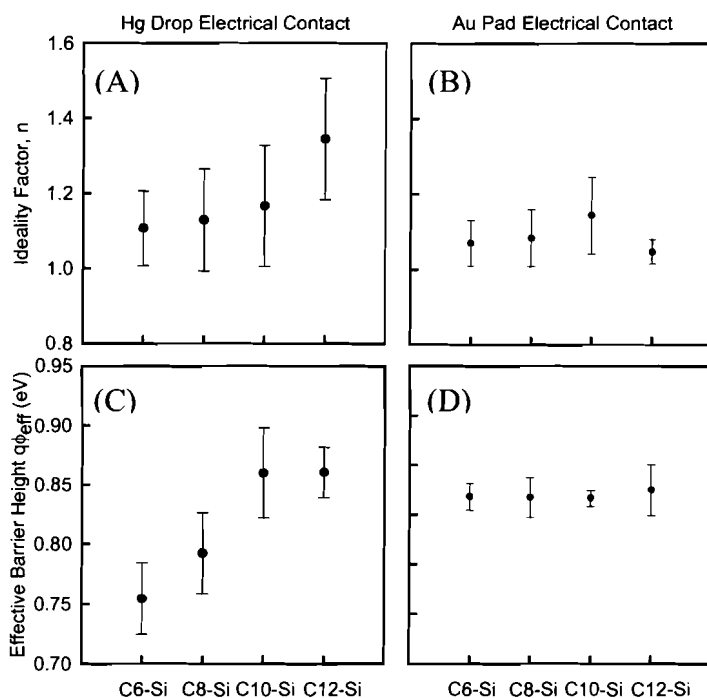


Figure 4-6 The effect of increasing chain length on the ideality factors and barrier heights of a series of n-alkyl-modified silicon surfaces (C6-Si, C8-Si, C10-Si, C12-Si) as measured by mercury drop (A and C) and gold pad (B and D) electrical contacts.

Figure 4-5 shows the effect of increasing chain-length on the current density vs. voltage behaviour of metal|monolayer-Si junctions as measured by mercury drop and gold pad electrodes. It can be seen that all of the junctions displayed rectifying behaviour. For junctions using mercury drop top electrodes, we can see that increasing the alkyl

chain length results in a decrease of current density for a given bias. As seen in figure 4-6, there is a clear trend: increasing the chain length increases the barrier height of the diode junction by roughly 0.3 eV /CH₂ unit on going from C6-C10 monolayers. Looking at equation 2.2, there are two contributions to the effective barrier height in an Schottky diode system: an intrinsic barrier due to the substrate, and an electron-tunnelling term. With non-penetrating mercury drop contacts, as the thickness of the monolayer increases, the barrier due to tunnelling across the monolayer increases (Figure 4-7). The experimentally determined values for the ideality factors and barrier heights are in agreement with literature data (except for C12-Si)³¹. These results demonstrate that by increasing the chain-length of the molecular insulating layer in a Hg|monolayer-Si junction, the insulating barrier to electron transport across the junction can be increased, allowing the barrier height of the diode junction to be tuned.

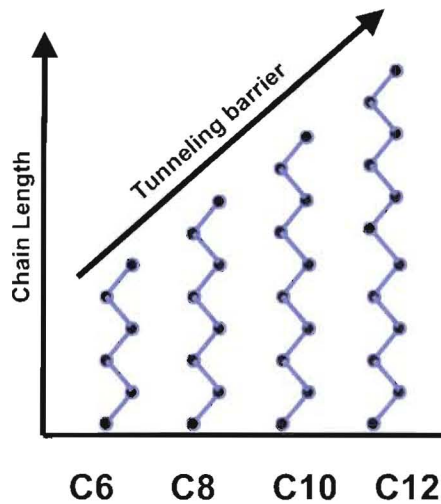


Figure 4-7 Diagram depicting the increasing tunnelling barrier on increasing the chain length of the monolayer in Hg|C_n-Si junctions, where n is the number of CH₂/CH₃ groups.

It is also of note, however, that increasing the chain length of the molecules in the monolayer from 10 to 12 carbons has a smaller effect on the barrier height than an increase from 6 to 10 carbons. A possible reason for this is that the longer chains may not remain rigidly packed, but rather begin to lie down parallel to the surface, resulting in thinner, less densely packed monolayers.

In stark contrast to the mercury drop *J-V* measurements, measurements performed using gold pad top electrodes showed almost no variation in the current density when varying the chain length of the molecules in the monolayer (figure 4-6): the extracted ideality factors and barrier heights for all of the junctions were approximately 1.05 and 0.83 eV, respectively. This lack of any significant change in the current density, coupled with the rectifying behaviour, confirms what was observed for H-Si, SiO₂-Si, and C10-Si samples, namely that the penetration of gold atoms into pinholes of the molecular layer during the deposition process shorts the circuit. It would also appear that the length of the molecules does not control the degree of gold penetration.

While these comparative *J-V* measurements demonstrate that gold does in fact penetrate the monolayer, the structure of the interface cannot be determined. The question still remains whether the gold simply disrupts the packing as seen by Jun et al for alkyl monolayers on silicon oxide³, or whether the direct thermal deposition actually destroys the monolayer in a fashion similar to that shown by Richter et al.²⁹ By using capacitance measurements, we are more clearly able to answer this question.

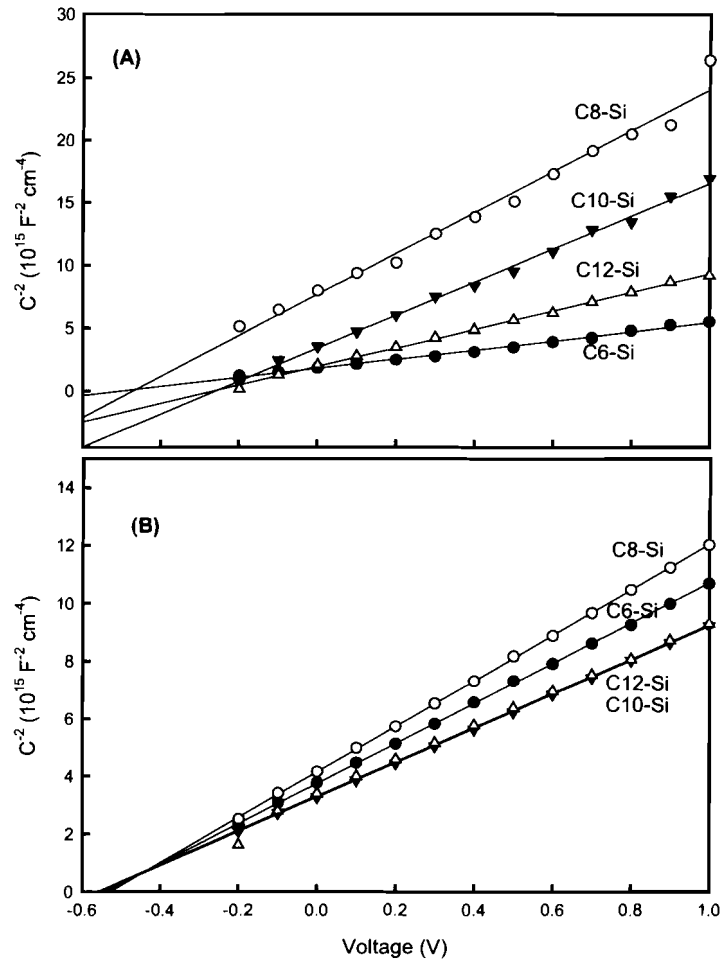


Figure 4-8 Mott-Schottky plots of a series of n-alkyl-modified silicon surfaces (C6-Si, C8-Si, C10-Si, and C12-Si) as measured by mercury drop (A) and gold pad (B) top electrical contacts.

Table 4-4 The calculated dopant density (N_d), flatband voltage (V_{do}) and barrier height ($q\phi_b$) of a series of n-alkyl silicon surfaces (C6-Si, C8-Si, C10-Si, and C12-Si) as measured by mercury drop and gold pad electrical contacts.

Sample	Mercury Drop			Gold Pad		
	$N_d / \times 10^{15} \text{ cm}^{-3}$	V_{do} / V	$q\phi_b / \text{eV}$	$N_d / \times 10^{15} \text{ cm}^{-3}$	V_{do} / V	$q\phi_b / \text{eV}$
C6-Si	3.36	0.50 ± 0.05	0.73 ± 0.06	1.7 ± 0.1	0.54 ± 0.01	0.79 ± 0.01
C8-Si	0.41 ± 0.24	0.39 ± 0.07	0.68 ± 0.07	1.4 ± 0.7	0.52 ± 0.03	0.80 ± 0.05
C10-Si	0.63 ± 0.22	0.35 ± 0.07	0.63 ± 0.07	2.1 ± 0.1	0.55 ± 0.02	0.79 ± 0.02
C12-Si	0.77 ± 0.18	0.37 ± 0.02	0.55 ± 0.04	2.0 ± 0.1	0.56 ± 0.01	0.80 ± 0.01

Table 4-3 shows the calculated values for V_{do} and $q\phi_b$ using data from the mercury drop and gold electrode Mott-Schottky plots. For mercury drop *M-S* measurements, all the samples (except C12-Si) return barrier heights of approximately 0.65 eV, consistent with literature reports for Hg|C10-Si junctions³². This result was expected because *M-S* measurements probe only the interface of monolayers of the same composition (straight-chain alkanes), made by the same reaction method, and similar surface densities would be expected to display similar interfacial electrical properties. The lower barrier height for C12-Si and the variability in the doping density among samples may be a result of changes in the structure of the monolayer⁵⁰.

For gold electrode *M-S* measurements, as was the case for the mercury drop electrodes, all of the junctions resulted in the same calculated barrier height. Once again, this makes sense if the method of monolayer preparation and the structures of the molecules are identical at the interface. The barrier height values determined with gold contacts are slightly higher than those with mercury. In the case of mercury, the metal forms an intimate contact, with the mercury droplet conforming to but not penetrating into the monolayer. In contrast, based on *J-V* measurements, gold appears to enter into the molecular layer and interacts with the silicon substrate. Further confirmation of this hypothesis rests with the fact that the barrier heights calculated from *M-S* measurements for the alkyl-modified silicon surfaces are the same as for the H-Si sample and as the values calculated from *J-V* measurements.

4.2.2 Nanoscale Electrical Characterization

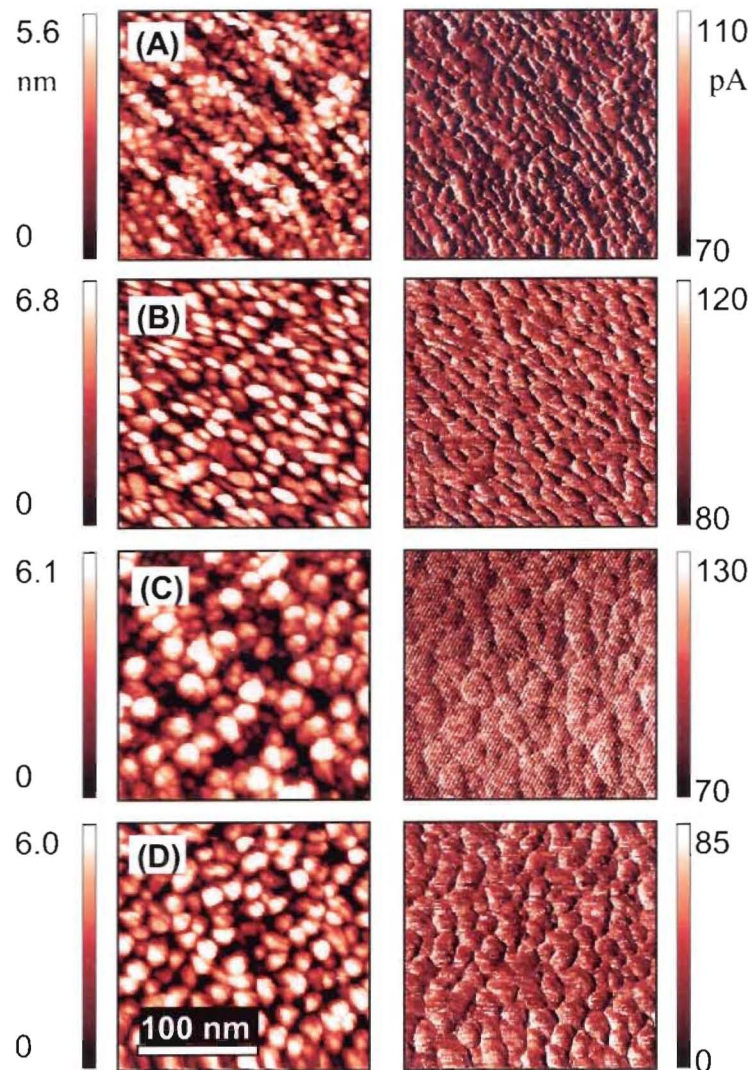


Figure 4-9 STM topography (in nm) and corresponding BEEM current images (in pA) for a series of $\text{Au}|n\text{-alkyl}$ monolayer-silicon junctions: $\text{Au}|\text{C}_6\text{-Si}$ (A), $\text{Au}|\text{C}_8\text{-Si}$ (B), $\text{Au}|\text{C}_{10}\text{-Si}$ (C), and $\text{Au}|\text{C}_{12}\text{-Si}$ (D).

The BEEM data shown in figures 4-9 (A) → (D) are remarkably similar. For all samples (C6-Si, C8-Si, C10-Si, C12-Si), the STM topography shows typical structures for thermally evaporated gold grains forming on the surface. As was seen for the reference $\text{Au}|\text{H-Si}$ junctions, the BEEM current images for (C6-C12)-Si all showed a

strong correlation between the STM topography and the collected BEEM current. Once again, the significance of this lack of lateral variation of these results is that the intervening molecular layer plays no part in the control over the BEEM current and hence the measured barrier heights. This indicates that the gold atoms are penetrating directly into the monolayer. Furthermore, because of the uniformity of the measured BEEM current throughout the sample, it can be seen that there is uniform mixing of the gold with the monolayer down to a scale of at least 15 nm.

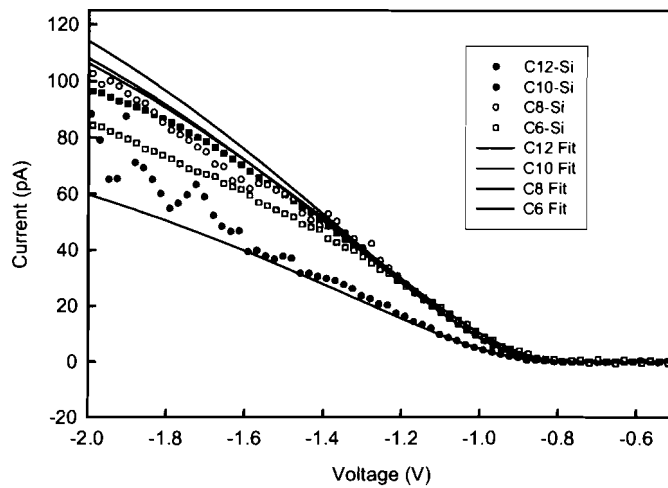


Figure 4-10 Static BEEM I - V curves for $\text{Au}|\text{C}6\text{-Si}$, $\text{Au}|\text{C}8\text{-Si}$, $\text{Au}|\text{C}10\text{-Si}$, and $\text{Au}|\text{C}12\text{-Si}$ along with theoretical fits, (solid lines), based on Bell-Kaiser theory.

The static BEEM I - V curves for the samples $\text{Au}|\text{C}6\text{-Si}$, $\text{Au}|\text{C}8\text{-Si}$, $\text{Au}|\text{C}10\text{-Si}$, and $\text{Au}|\text{C}12\text{-Si}$ shown in figure 4-9 confirm what was seen for the macroscale gold J - V measurements, that is, there is no chain-length dependence of the barrier height of the $\text{Au}|\text{monolayer-Si}$ junction. The threshold voltage for all of the samples was approximately 0.82 eV, corresponding to a direct $\text{Si}|\text{Au}$ interface. Furthermore, it can be

seen that the magnitude of the BEEM current is almost identical amongst the samples, suggesting that the effectiveness of insulation is the same for all of the molecules.

4.3 Electrical Properties of Diode Junctions Constructed from Thiol- and Thioacetate-Terminated Monolayers on Silicon

In addition to the promise of providing materials with greater insulating properties than those currently available, molecular modification of semiconducting materials is offering the possibility of directly incorporating sensing capabilities in their surfaces. This would allow a combination of a wide variety of chemical and electronic properties of a large number of available organic molecules with the well-characterized electronic behaviour and advanced fabrication techniques for semiconducting materials. The simplest such systems have different functional groups (e.g., -OH, -COOH, -COOR) at the terminal ends of alkyl chains attached to semiconducting materials²⁰.

We chose to fabricate a silicon-monolayer system incorporating thioacetate and thiol functionalities at the monolayer surface. This type of junction has not been previously characterized when covalently linked through a carbon-silicon. Several factors influenced the selection of thioacetate and thiol functionalities for these studies. First we wanted to address the issue of metal penetration into the alkyl monolayers attached to silicon. Due to the interaction between sulfur groups and metals, it was hypothesized that the presence of these functionalities on the surface may prevent or minimize the extent of such penetration. Secondly, because the small size of the thioacetate functionality relative to the footprint of the molecule (the effective cross section of a molecule on the surface), the density of molecule packing on the silicon surface was expected to be similar to that

of n-alkyl monolayers. Furthermore, the presence of a thiol terminus opens up the possibility to further modify the silicon surface.

Due to the reactivity of thiol-terminated molecules toward bare silicon surfaces and toward themselves (formation of disulfide linkages), as well as the stability of the thiol group, direct attachment of a thiol-terminated alkyl chain onto silicon was not possible. Therefore, a two-step route was designed: a thioacetate-terminated surface was first prepared via thermal hydrosylation of unoxidized silicon, followed by *in-situ* deprotection to yield the desired thiol-terminated silicon surface.

4.3.1 Macroscale Measurements

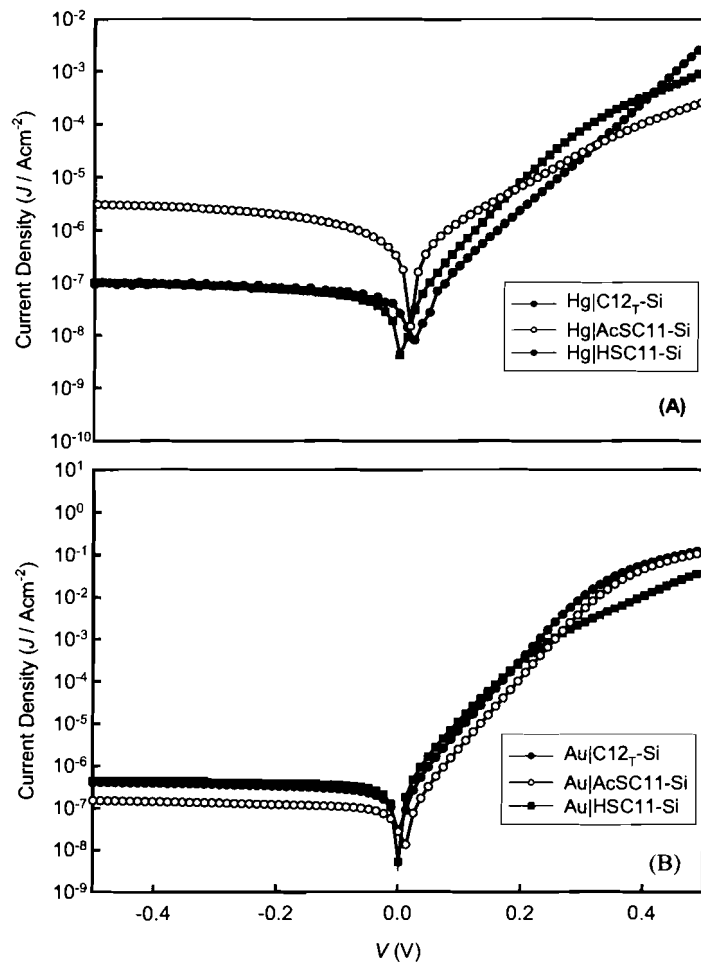


Figure 4-11 Log current density vs. voltage for $\text{Au|C12}_T\text{-Si}$, Au|AcSC11-Si , and Au|HSC11-Si as measured by mercury drop (A) and gold pad (B) top electrical contacts.

Table 4-5 Ideality factors (n) and barrier heights ($q\phi_{eff}$) for C12_T-Si, AcSC11-Si, and HSC11-Si samples as measured by mercury drop and gold pad top electrical contacts.

Sample	Mercury Drop		Gold Pad	
	n	$q\phi_{eff}$ / eV	n	$q\phi_{eff}$ / eV
C12 _T -Si	1.45±0.16	0.89±0.04	1.03±0.02	0.81±0.01
AcSC11-Si	1.31±0.03	0.88±0.03	1.08±0.08	0.81±0.04
HSC11-Si	2.56±0.03	0.79±0.03	1.02±0.08	0.84±0.06

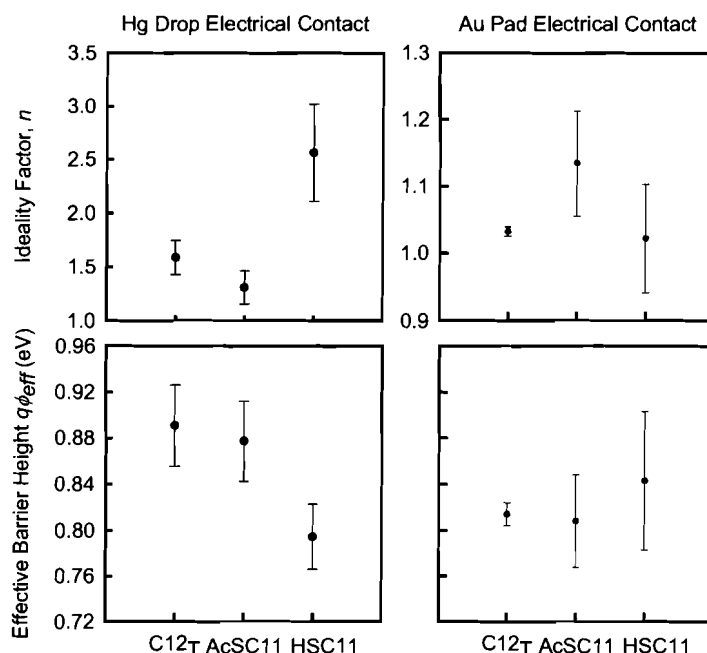


Figure 4-12 The effect of terminal monolayer functionality on the ideality factors and barrier heights of C12_T-Si, AcSC11-Si, and HSC11-Si samples as measured by mercury drop (A and C) and gold pad (B and D) electrical contacts.

Figure 4-10 shows characteristic current density plots of dodecyl (C12_T-Si), ω -undecenyl thioacetate (AcSC11-Si), and ω -undecenyl thiol (HSC11-Si) modified silicon surfaces created via thermal hydrosilylation of unoxidized silicon measured with mercury drop and gold pad electrical contacts. Because the method of attachment of the molecules

onto the silicon surface differed from that of the series of n-alkyl-modified monolayers (C6-Si, C8-Si, C10-Si, and C12-Si), a C12_T-Si monolayer was created as control for comparison.

For the mercury drop measurements, C12_T-Si demonstrated rectifying behaviour with higher ideality factors n but similar barrier heights as compared to the C12-Si sample formed via Grignard reaction ($q\phi_{eff} = 1.45 \pm 0.16$ and 0.89 ± 0.04 eV respectively). While the ideality factor is somewhat higher, it is not outside a reasonable range, and the barrier heights are comparable within experimental error.

The AcSC11-Si sample, which has a slightly longer chain length than C12_T-Si (16.8 Å vs. 13.7 Å), also displays rectifying behaviour, with similar ideality factors and barrier height as the C12_T-Si sample ($n = 1.31 \pm 0.15$, $q\phi_{eff} = 0.88 \pm 0.03$ eV). This would seem to indicate that the presence of the thioacetate functional group does not affect the electronic properties of the silicon-monolayer device. In contrast, the HSC11-Si sample prepared via deprotection of a AcSC11-Si sample showed a decrease of the barrier height to 0.79 ± 0.03 eV. Since the C11SH molecule at 14.0 Å is not significantly shorter than the C12 or C11SAC molecules, chain length cannot be the source of this decrease. In fact, according to the trend seen for the barrier heights of n-alkyl-modified monolayers on silicon, the HSC11-Si sample would appear to have the same length as an 8-carbon chain molecule, which is clearly not the case. The packing density of the molecules is also not in question as HSC11-Si surface is derived from AcSC11-Si, which did not show a similar reduction in barrier height. Several studies have demonstrated that the barrier height changes with the dipole moment of the molecules on the surface.^{50, 51} Cahen et al.⁵² quantified this effect by adding a dipole moment contribution term to equation 1.1 so

that the barrier height could now be defined as the difference in the work function of the metal and the electron affinity of the semiconductor as influenced by the dipole moment of the molecular layer:

$$q\phi_b = q[\varphi_m - (\chi_s + \phi_{dipole})] \quad \text{Equation 4.1}$$

where the dipole contribution, ϕ_{dipole} , is defined as:

$$\phi_{dipole} = \frac{N\mu \cos \theta}{\epsilon \epsilon_0} \quad \text{Equation 4.2}$$

Figure 4-10 also shows the behaviour of C12_T-Si, AcSC11-Si, and HSC11-Si as measured with gold electrodes. As was seen with mercury droplets as top electrical contacts, the measurements with gold pads on C12_T-Si showed no difference in barrier height relative to C12-Si formed via Grignard reaction. Also similar to the mercury drop measurements was the lack of a significant change in the barrier heights of C12_T-Si and AcSC11-Si. In contrast to the mercury drop measurements, however, the HSC11-Si did not show a decrease in the barrier height. In fact, all C12_T-Si, AcSC11-Si, and HSC11-Si samples showed ideality factors and barrier heights identical to H-Si, as seen in the series of alkyl monolayers on silicon made via Grignard reactions. This demonstrates that on the scale at which these measurements were carried out (3000 μm gold contacts), the barrier height of a Au|monolayer-Si junction is independent of both monolayer chain length and terminal functional group. This indicates that the direct thermal deposition of metals onto organic molecules covalently linked to a silicon substrate via Si-C bonds results in widespread shorting of the junctions.

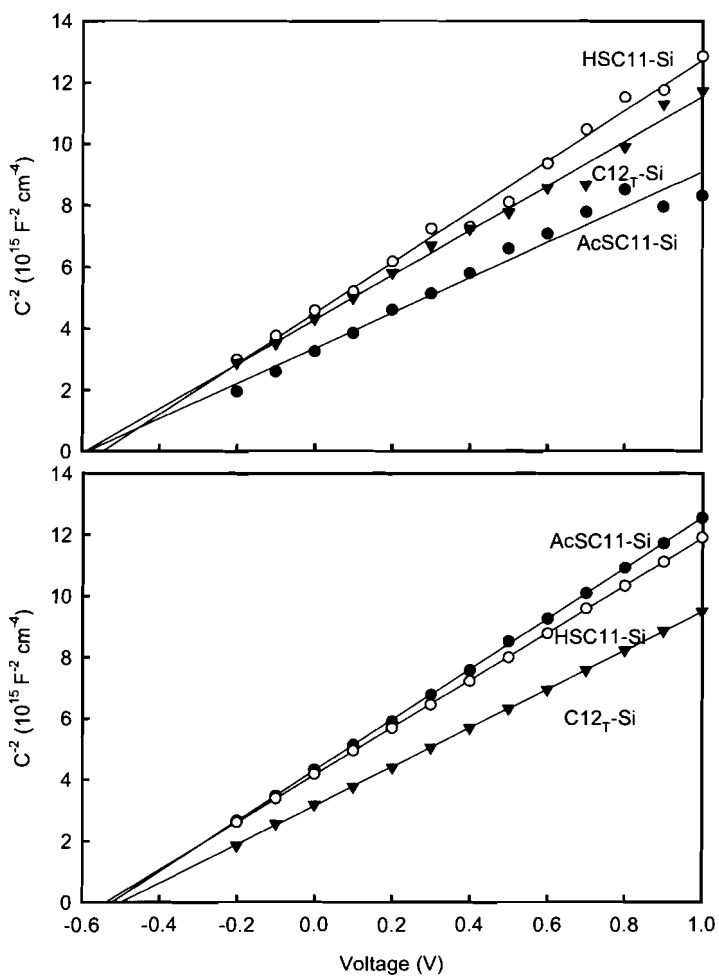


Figure 4-13 Mott-Schottky plots depicting the behaviour of n-alkyl ($C_{12T}-Si$), and functionalised alkyl monolayers (AcSC11-Si and HSC11-Si) as measured by mercury drop (A) and gold pad (B) top electrical contacts.

Table 4-6 The calculated dopant density (N_d), flatband voltage (V_{do}), and barrier height ($q\phi_b$) of n-alkyl (C12_T-Si), and functionalised alkyl monolayers (AcSC11-Si and HSC11-Si) as measured by mercury drop and gold pad electrical contacts.

Sample	Mercury Drop			Gold Pad		
	$N_d / \times 10^{15} \text{ cm}^{-3}$	V_{do} / V	$q\phi_b / \text{eV}$	$N_d / \times 10^{15} \text{ cm}^{-3}$	V_{do} / V	$q\phi_b / \text{eV}$
AcSC11-Si	2.1±0.16	0.59±0.16	0.83±0.16	1.9±0.1	0.50±0.01	0.74±0.01
HSC11-Si	1.47±0.16	0.55±0.16	0.79±0.16	1.6±0.2	0.48±0.05	0.74±0.05
C12 _T -Si	1.67±0.16	0.59±0.16	0.84±0.16	1.8±0.3	0.53±0.03	0.78±0.03

As was the case for monolayers made via Grignard reactions, all monolayers made using the thermal hydrosilylation of unoxidized silicon gave similar barrier heights. The magnitude of $q\phi_b$ calculated from *M-S* measurements, however, was approximately 0.2 eV higher than the values obtained for monolayers made by Grignard reactions. Because *M-S* measurements probe the silicon interface, an increase in interface states, as evidenced by increased ideality factors can result in V_{do} deviations as well as increased barrier heights. On comparing the ideality factors, for diodes made via thermal and Grignard reactions, we see that there is an average increase of 0.3. One possible explanation is that the thermal reaction results in an increase in interface states due to a greater number of dangling silicon bonds.

All *M-S* measurements for C12_TSi, AcSC11-Si, and HSC11-Si using the thermally evaporated gold contacts resulted in similar barrier heights of approximately 0.77 eV, which is within the range of a direct Si|Au contact. This indicates that the presence of functional groups on the terminal end of the monolayer does not prevent the penetration of gold into the molecular layer and the metal's interaction with the silicon interface. The difference between the mercury droplet and gold *M-S* measurements may

lie in the fact that the gold penetrates uniformly into the monolayer. The effect of the gold contacting the silicon surface may override any other surface effects due to monolayer formation.

4.3.1 Nanoscale Electrical Measurements

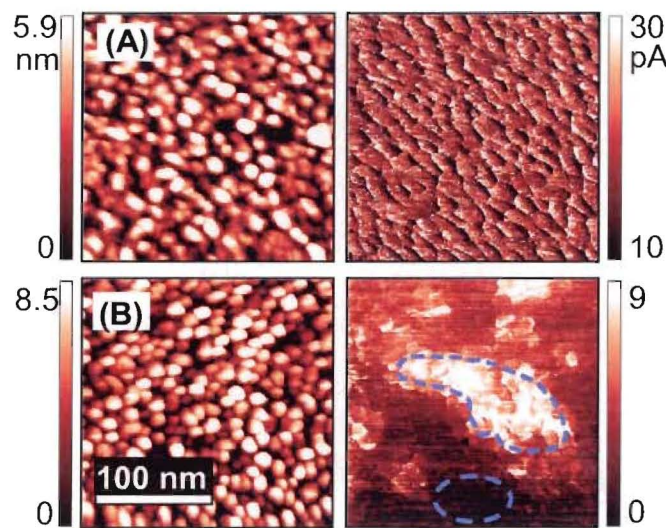


Figure 4-15 STM topography and corresponding BEEM current images for (A) AcSC11-Si and (B) HSC11-Si.

Figure 4-14 shows typical STM and corresponding BEEM current images for AcSC11-Si and HSC11-Si. The AcSC11-Si samples showed the same behaviour as n-alkyl monolayers on silicon, that is, a uniform BEEM threshold throughout the sample and a direct correlation between BEEM current magnitude and STM topography, indicating gold metal penetration uniformly throughout the molecular film. This indicates a laterally uniform interfacial structure, which is not affected by the presence of the thioacetate terminal functional group.

The HSC11-Si samples, however, showed a remarkably different behaviour from n-alkyl-Si and AcSC11-Si. While the STM topography image showed the typical

morphology of gold grains deposited via a thermal evaporation, the BEEM current did not display a direct correlation with the STM topography in all areas. As shown in figure 4-14, the BEEM image showed some regions with higher currents, which correspond closely to the STM topography, while other areas displayed greatly reduced or no BEEM current signal. These variations in the lateral BEEM current images can be interpreted as a partially thiolated surface, in which the probability of gold penetrating into the monolayer is reduced in regions containing terminal -SH functional groups.

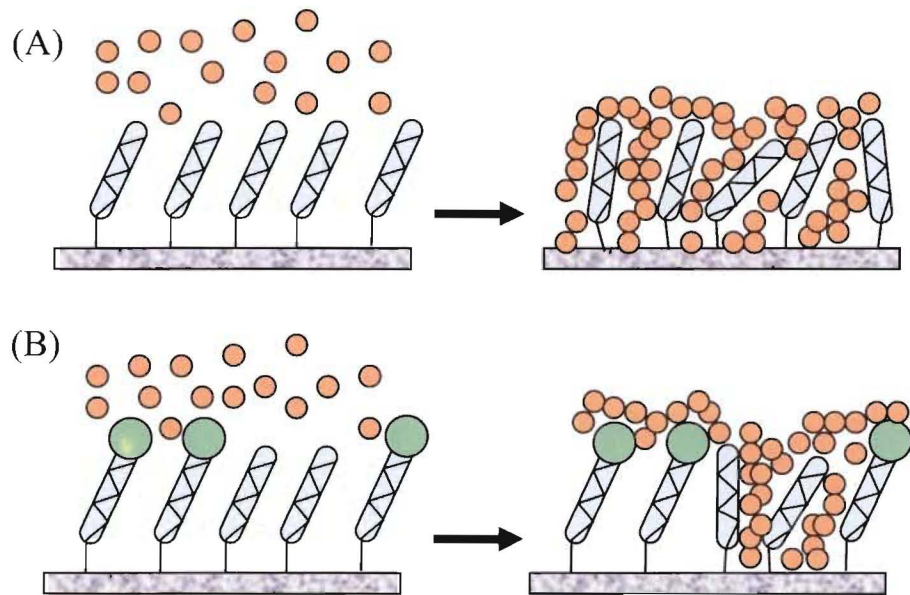


Figure 4-16 Illustration of the behaviour of gold atoms upon thermal deposition onto (A) methyl-terminated (B) (partially) thiol-terminated monolayers on silicon. Larger green circles represent terminal thiol groups, while smaller orange circles represent gold atoms.

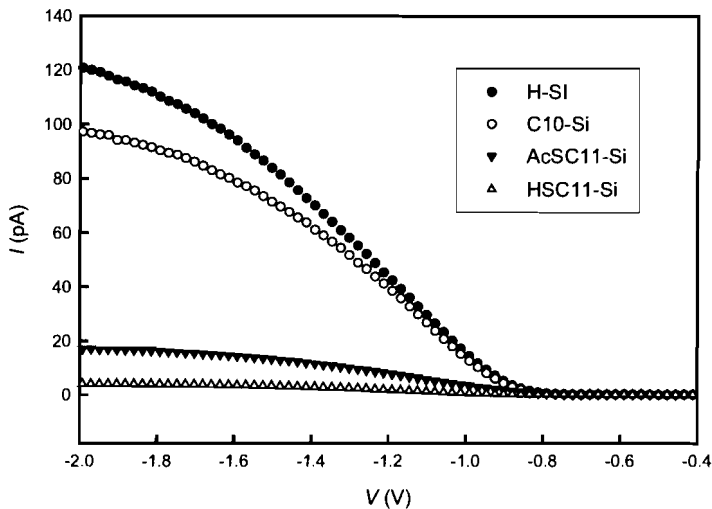


Figure 4-17 BEEM I - V overlay of Au|H-Si, Au|C10-Si, Au|AcSC11-Si, and Au|HSC11-Si showing the decreasing magnitude of BEEM current on going from un-oxidized, to n-alkyl protected, to alkyl-thioacetate protected, to alkyl-thiol protected silicon.

The threshold potential extracted from BEEM I - V curves (figure 4-16) shows no variation between H-Si, n-alkyl-Si, AcSC11-Si, and HSC11-Si, with all samples giving an identical value of -0.82 ± 0.02 V. This indicates that gold does in fact penetrate all of the monolayers and that the threshold is dominated by gold directly in contact with the silicon substrate. Similar to the reduction in BEEM current magnitude on going from Au|H-Si to Au|C10-Si shown in the previous section, a further reduction was observed on going to Au|AcSC11-Si and Au|HSC11-Si junctions. Because there was no change in the interfacial barrier height, this reduction in current intensity must be a result of molecular scattering due to the different terminal functionalities, or of interactions between the deposited gold atoms and the terminal functional groups.

4.3.2 Transmission Electron Microscopy

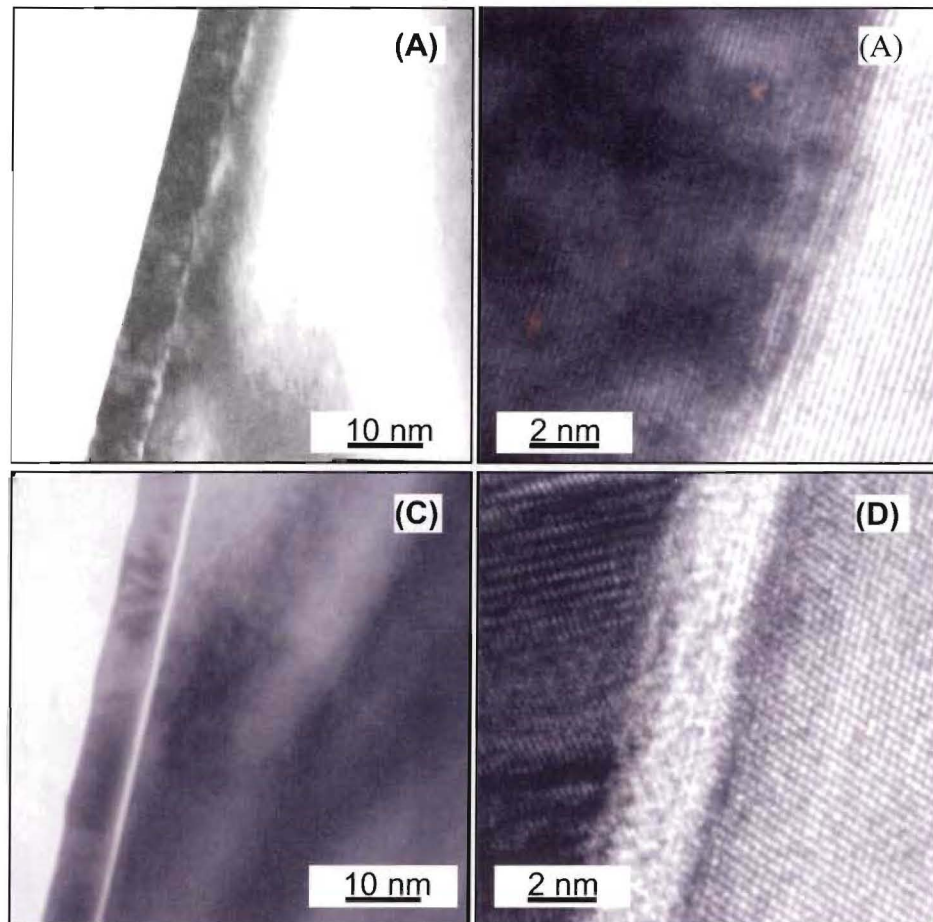


Figure 4-18 TEM cross-sectional images of AcSC11-Si (A and B) and HSC11-Si (C and D) samples taken down the (112) and (110) dipoles respectively.

TEM cross-section images of Au|C10-Si and Au|HSC11-Si samples taken with the beam parallel to either the [112] substrate direction (a (112) pole) or the perpendicular [011] substrate direction (a (011) pole) are shown in Figure 4-17. A clear Au|Si contact is observed for the Au|C10-Si junction, while for the Au|HSC11-Si junction an interfacial layer is observed with a variable thickness of 2.0 ± 0.5 nm, consistent with the maximum length of the molecules. The brighter contrast of the interfacial layer indicates a lower

mass density. For part of the interface, gold directly contacts with silicon but for other regions, a distinguishable interlayer without gold lattice fringes is clearly observed.

CHAPTER 5: CONCLUDING REMARKS AND FUTURE WORK

The use of covalently attached organic monolayers on silicon surfaces for the construction of hybrid molecule-semiconductor devices continues to be a hotly debated topic in the emerging field of molecular electronic devices. To that end, n-alkyl, thioacetate and thiol-terminated monolayers were prepared on silicon substrates via covalent Si-C bonding, and their effects were evaluated at both the macroscale using mercury drop electrodes and thermally deposited gold pads, and the nanoscale using BEEM and TEM. Mercury drop J - V measurements demonstrate that not only can bare silicon surfaces be passivated with n-alkyl monolayers, but also that the barrier height can be tuned by varying the chain length of the alkyl groups. It was also shown that the functionalization of the end groups of the monolayers could be used for controlling the electrical properties; with reduction of barrier height on introduction of a polar alkyl thiol monolayer when measured with mercury drop electrodes.

In contrast to mercury drop measurements, macroscale gold J - V measurements showed neither chain length, nor terminal group dependence of the electrical properties of the diode junctions. Furthermore, the behaviour of both n-alkyl and ω -functionalised monolayers corresponded directly to direct Si|Au contacts, indicating penetration of the molecular layer by the deposited gold atoms.

Nanoscale BEEM and TEM measurements support the observation of shorting of all of the molecularly modified silicon diodes when using thermally deposited gold electrodes, with laterally uniform BEEM current images observed for n-alkyl and thioacetate-terminated monolayers down to a scale of ~20 nm. BEEM *I-V* scans show, however, a decrease in the BEEM current transmission probability on going sequentially from hydrogen-terminated samples, n-alkyl monolayers, thioacetate-terminated monolayers, and to thiol-functionalised monolayers. Furthermore, lateral variations in BEEM current images on the scale of 20 – 200 nm were detected for thiol-functionalized monolayers. Combined, these data suggest that while thermally deposited gold atoms penetrate the monolayers, they do not remove all of the covalently attached molecules, and the presence of thiol groups decreases the probability of gold atom penetration.

These studies point to several possible avenues for future explorations. The direct deposition of metals onto as prepared monolayers on silicon would not be of practical use due to the effect of metal penetration. One option is the introduction of larger protecting groups, such as gold nanoparticles immobilized on thiol-terminated monolayers on silicon (Figure 5-1). Another option is to forgo thermal deposition for a different method of metal contact formation such as nano-transfer printing (nTP) which involves stamping the metal film onto the thiol-terminated monolayer surface.

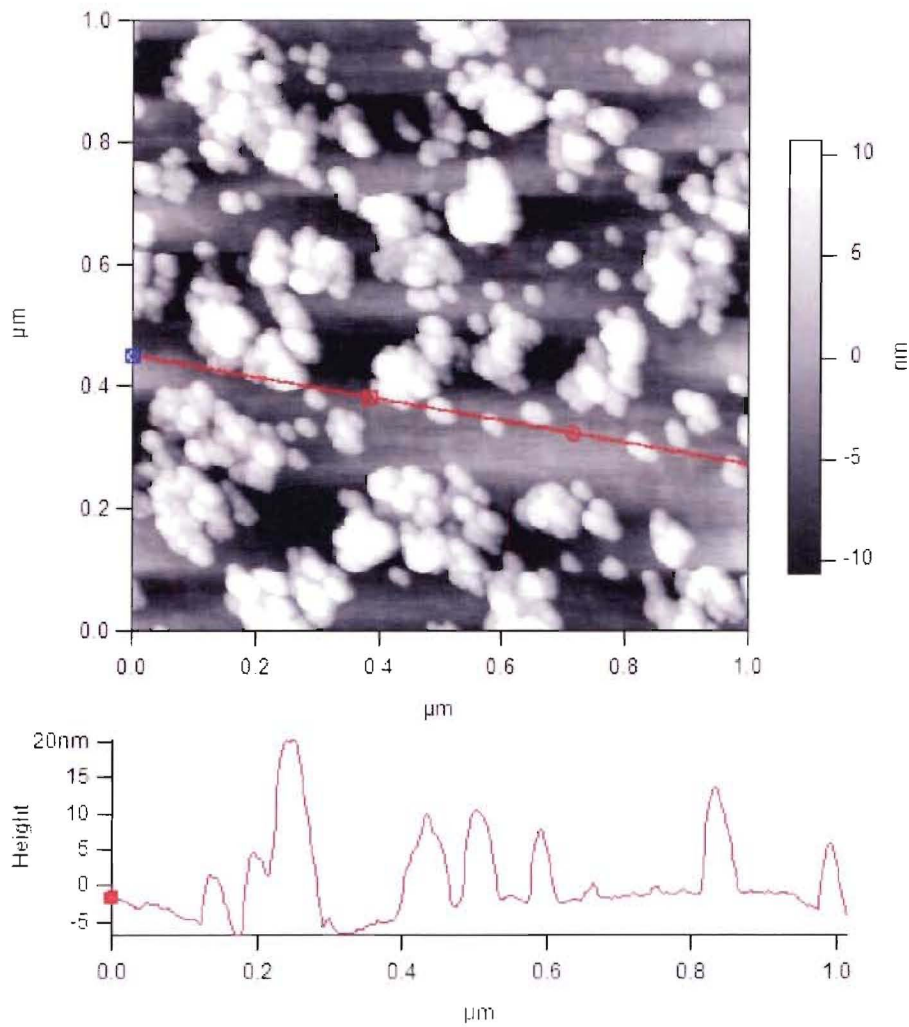


Figure 5-1 AFM image and associated line profile of a HSC11-Si sample incubated with a solution of 10 nm gold particles.

REFERENCES:

- (1) Tulevski, G. S.; Miao, Q.; Fukuto, M.; Abram, R.; Ocko, B.; Pindak, R.; Steigerwald, M. L.; Kagan, C. R.; Nuckolls, C. *J. Am. Chem. Soc.* 2004, **126**, 15048-15050.
- (2) Qi, P.; Javey, A.; Rolandi, M.; Wang, Q.; Yenilmez, E.; Dai, H. *J. Am. Chem. Soc.* 2004, **126**, 11774-11775.
- (3) Jun, Y.; Zhu, X. Y. *Journal of the American Chemical Society* 2004, **126**, 13224-13225.
- (4) Ng, M. K.; Lee, D. C.; Yu, L. *J. Am. Chem. Soc.* 2002, **124**, 11862-11863.
- (5) R. Lloyd Carroll, C. B. G. *Angewandte Chemie International Edition* 2002, **41**, 4378-4400.
- (6) Whitesides, G. M. *MRS Bulletin* 2002, **27**, 56-65.
- (7) Braun, F. *Poggendorff's Annalen* 1874, **153**, 556.
- (8) Schottky, W. S., R.; Waibel, F.; *Hochfrequenztechnik* 1931, **37**, 162.
- (9) Schottky, W. *Naturwissenschaften* 1938, **26**, 843.
- (10) Schottky, W. *Naturwissenschaften* 1938, **26**, 843.
- (11) Mott, N. F. *Proc. Cambridge Phil. Soc.* 1938, **34**, 568-572.
- (12) Mott, N. F. *Cambridge Philosophical Society* 1938, **4**, 568.
- (13) Sze, S. M. *Physics of Semiconductor Devices*; John Wiley & Sons: New York, 1981.
- (14) Turner, M. J.; Rhoderick, E. H. *Solid-State Electronics* 1968, **11**, 291-300.
- (15) Newman, N.; Spicer, W. E.; Kendelewicz, T.; Lindau, I. *Journal of Vacuum Science & Technology B: Microelectronics and Nanometer Structures* 1986, **4**, 931-938.
- (16) Newman, N.; Kendelewicz, T.; Bowman, L.; Spicer, W. E. *Applied Physics Letters* 1985, **46**, 1176-1178.
- (17) Bardeen, J. *Physical Review* 1947, **71**, 717.
- (18) Heine, V. *Physical Review* 1965, **138**, A1689.
- (19) Linford, M. R.; Chidsey, C. E. D. *Journal of the American Chemical Society* 1993, **115**, 12631-12632.
- (20) Buriak, J. M. *Chem. Rev.* 2002, **102**, 1271-1308.
- (21) Sung, M. M.; Kluth, G. J.; Yauw, O. W.; Maboudian, R. *Langmuir* 1997, **13**, 6164-6168.
- (22) Terry, J.; Linford, M. R.; Wigren, C.; Cao, R.; Pianetta, P.; Chidsey, C. E. D. *Applied Physics Letters* 1997, **71**, 1056-1058.
- (23) Cicero, R. L.; Linford, M. R.; Chidsey, C. E. D. *Langmuir* 2000, **16**, 5688-5695.
- (24) Song, J. H.; Sailor, M. J. *Journal of the American Chemical Society* 1998, **120**, 2376-2381.
- (25) Kim, N. Y.; Laibinis, P. E. *Journal of the American Chemical Society* 1999, **121**, 7162-7163.
- (26) Linford, M. R.; Fenter, P.; Eisenberger, P. M.; Chidsey, C. E. D. *Journal of the American Chemical Society* 1995, **117**, 3145-3155.
- (27) de Villeneuve, C. H.; Pinson, J.; Bernard, M. C.; Allongue, P. *Journal of Physical Chemistry B* 1997, **101**, 2415-2420.

- (28) Li, W.; Kavanagh, K. L.; Matzke, C. M.; Talin, A. A.; Leonard, F.; Faleev, S.; Hsu, J. W. P. *Journal of Physical Chemistry B* 2005, *109*, 6252-6256.
- (29) Richter, C. A.; Hacker, C. A.; Richter, L. J. *Journal of Physical Chemistry B* 2005, *109*, 21836-21841.
- (30) Richter, L. J.; Richter, C. A.; Hacker, C. A. *Abstracts of Papers, 229th ACS National Meeting, San Diego, CA, United States, March 13-17, 2005* 2005, COLL-360.
- (31) Liu, Y.-J.; Yu, H.-Z. *ChemPhysChem* 2002, *3*, 799-802.
- (32) Liu, Y.-J.; Yu, H.-Z. *ChemPhysChem* 2003, *4*, 335-342.
- (33) Liu, Y.-J.; Yu, H.-Z. *Journal of Physcial Chemistry B* 2003, *107*, 7803-7811.
- (34) Boukherroub, R.; Morin, S.; Bensebaa, F.; Wayner, D. D. M. *Langmuir* 1999, *15*, 3831-3835.
- (35) Linford, M. R.; Fenter, P.; Eisenberger, P. M.; Chidsey, C. E. D. *J. Am. Chem. Soc.* 1995, *117*, 3145-3155.
- (36) Balachander, N.; Sukenik, C. N. *Langmuir* 1990, *6*, 1621-1627.
- (37) Bell, L. D.; Kaiser, W. J. *Physical Review Letters* 1988, *61*, 2368.
- (38) Fowell, A. E.; Williams, R. H.; Richardson, B. E.; Shen, T. H. *Semiconductor Science and Technology* 1990, *5*, 348-350.
- (39) Kaiser, W. J.; Bell, L. D.; Hecht, M. H.; Grunthaner, F. J., BOZEMAN, MONTANA, USA 1989; AVS; 945-949.
- (40) Tivarus, C.; Pelz, J. P.; Hudait, M. K.; Ringel, S. A. *Applied Physics Letters* 2005, *87*, 182105-182103.
- (41) Rhoderick, E. H. W., R.H.; *Metal-Semiconductor Contacts*, 2 ed.; Oxford University Press: New York, 1998.
- (42) Kaiser, W. J.; Bell, L. D. *Physical Review Letters* 1988, *60*, 1406-1409.
- (43) Coates, J. *Interpretation of Infrared Spectra, A Practical Approach*; John Wiley & Sons Ltd.: Chichester, 2000.
- (44) Seitz, O.; Bocking, T.; Salomon, A.; Gooding, J. J.; Cahen, D. *Langmuir* 2006, *22*, 6915-6922.
- (45) Hales, W. B. *Physical Review* 1928, *32*, 950.
- (46) Allen, F. G.; Gobeli, G. W. *Physical Review* 1962, *127*, 150.
- (47) Varma, R. R.; McKinley, A.; Williams, R. H.; Higginbotham, I. G. *Journal of Physics D: Applied Physics* 1977, *10*, L171-L174.
- (48) Schowalter, L. J.; Lee, E. Y. *Physical Review B* 1991, *43*, 9308.
- (49) Grupp, C.; Taleb-Ibrahimi, A. *Physical Review B* 1998, *57*, 6258.
- (50) A. Salomon, D. C. S. L. J. T. V. B. E. C. D. F. *Advanced Materials* 2003, *15*, 1881-1890.
- (51) Ashkenasy, G.; Cahen, D.; Cohen, R.; Shanzer, A.; Vilan, A. *Accounts of Chemical Research* 2002, *35*, 121-128.
- (52) Vilan, A.; Shanzer, A.; Cahen, D. *Nature (London)* 2000, *404*, 166-168.

APPENDIX

In performing electrical measurements of solid-state electronic devices such as metal|monolayer-semiconductor diodes, it is necessary to recognize that there can be a range of sample variability, depending on the individual sample characteristics, that may influence parameters such as the ideality factor and effective barrier height of the diode include the extent of the monolayer coverage on the semiconductor surface. Some of these factors include: the number of dangling bonds at the interface, trapped charges at the interface, defects in the underlying semiconductor crystal lattice, local dopant concentration, extent of oxidation of the surface, as well as the extent of metal interaction with the semiconductor and monolayer. In order to extract parameters typical of one system, it is necessary to carry out a large number of measurements on a large number of discrete samples. Figure A-1 shows overlay J-V plots for Hg|C10-Si and Au|C10-Si samples. The ideality factors and barrier heights extracted from these plots are shown in figure A-2.

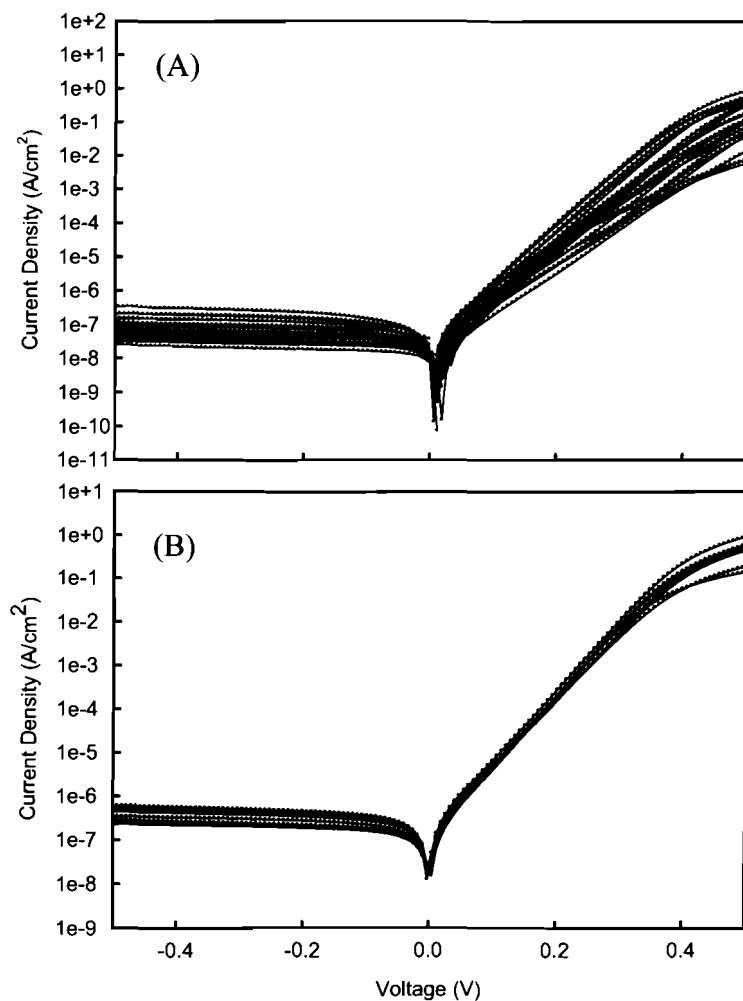


Figure A-1 Overlay of (A) 66 J - V plots for Hg|C10-Si junctions and (B) 33 J - V plots for Au|C10-Si junctions.

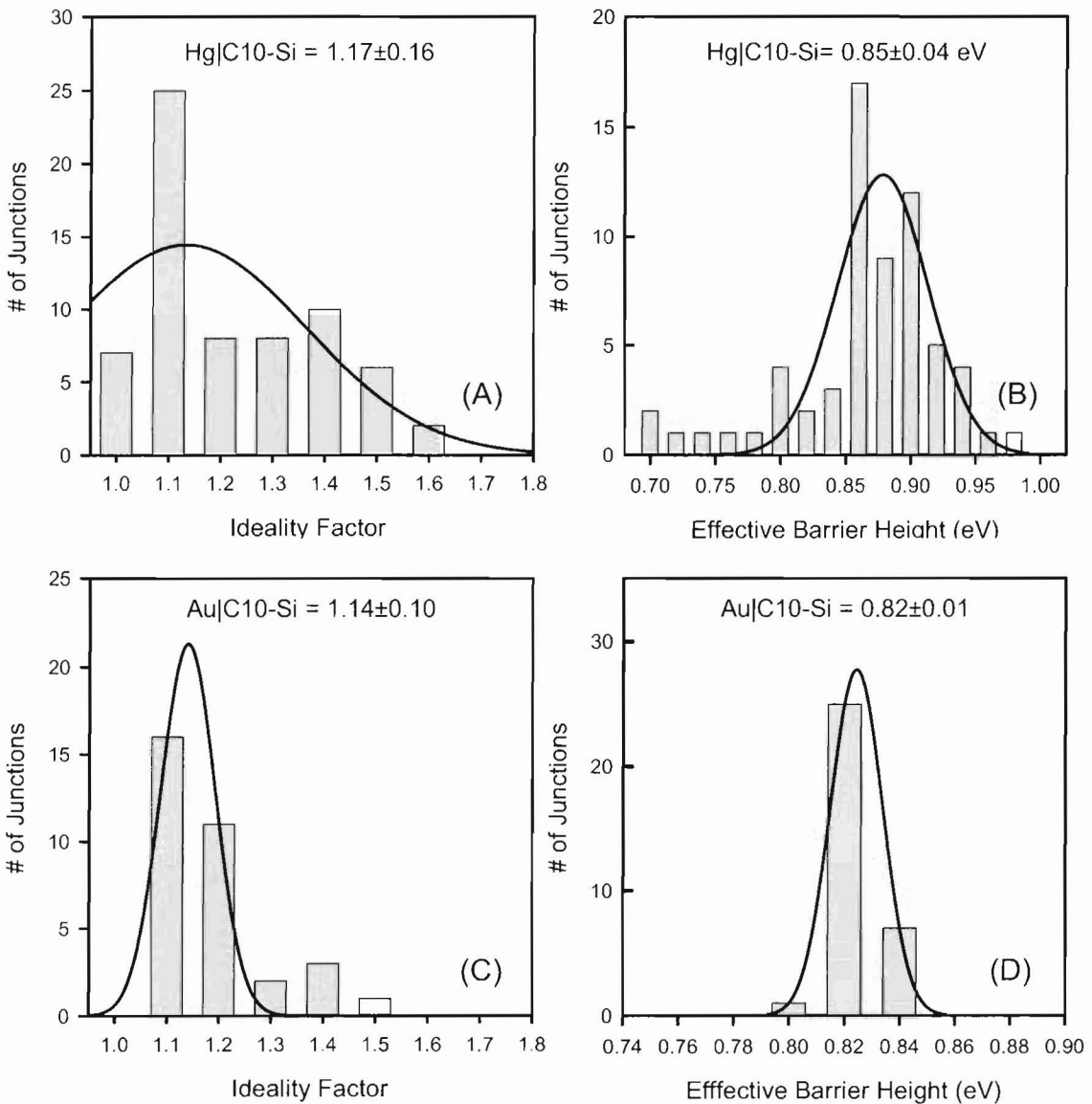


Figure A-2 Distributions of the ideality factors and barrier heights for extracted from current density–voltage (J - V) curves. Distribution of the (A) ideality factors and (B) barrier heights of 66 independent Hg|C10-Si junctions from 12 C10-Si samples. Distribution of ideality factors (C) and barrier heights (D) of 33 Au|C10-Si junctions from 7 C10-Si samples.